Review article

Multiscale modeling of electrolytes in porous electrode: From equilibrium structure to non-equilibrium transport

Haolan Tao [a], Cheng Lian [a,b,c,*], Honglai Liu [a,b,*]

[a] State Key Laboratory of Chemical Engineering and Shanghai Engineering Research Center of Hierarchical Nanomaterials, School of Chemical Engineering, East China University of Science and Technology, Shanghai, 200237, China
[b] School of Chemistry and Molecular Engineering, East China University of Science and Technology, Shanghai, 200237, China
[c] Institute for Theoretical Physics, Center for Extreme Matter and Emergent Phenomena, Utrecht University, Princetonplein 5, 3584 CC Utrecht, the Netherlands

Abstract

Understanding the mechanisms and properties of various transport processes in the electrolyte, porous electrode, and at the interface between electrode and electrolyte plays a crucial role in guiding the improvement of electrolytes, materials and microstructures of electrode. Nanoscale equilibrium properties and nonequilibrium ion transport are substantially different to that in the bulk, which are difficult to observe from experiments directly. In this paper, we introduce equilibrium and no-equilibrium thermodynamics for electrolyte in porous electrodes or electrolyte−electrode interface. The equilibrium properties of electrical double layer (EDL) including the EDL structure and capacitance are discussed. In addition, classical non-equilibrium thermodynamic theory is introduced to help us understand the coupling effect of different transport processes. We also review the recent studies of nonequilibrium ion transport in porous electrode by molecular and continuum methods, among these methods, dynamic density functional theory (DDFT) shows tremendous potential as its high efficiency and high accuracy. Moreover, some opportunities for future development and application of the non-equilibrium thermodynamics in electrochemical system are prospected.

1. Introduction

Developing excellent porous electrode materials and electrolytes has attracted intense interest in improving the promising applications for energy storage and conversion, such as supercapacitors and batteries [1−5]. Due to the advantages of high power density, long cycling life and operational safety [6], supercapacitors are very outstanding electrochemical energy storage devices with high power density, but limited by the poor energy density, which is far less than that of batteries [7−9]. Research on supercapacitors can be classified into two categories based on their energy storage methods: electrochemical double layer capacitance (EDLC) [10−12], which is originated from the EDL on the electrode surface, and pseudocapacitance [4,13], which results from the quickly reversible Faradaic reactions on the surface of electrode. For a supercapacitor, the energy density (E) is calculated by:

$$E = \frac{CU^2}{2}, \tag{1}$$

and the maximum power density is expressed as:

* Corresponding authors. State Key Laboratory of Chemical Engineering and Shanghai Engineering Research Center of Hierarchical Nanomaterials, School of Chemical Engineering, East China University of Science and Technology, Shanghai, 200237, China.
  E-mail addresses: liancheng@ecust.edu.cn (C. Lian), hlliu@ecust.edu.cn (H. Liu).

$$P_{max} = \frac{U^2}{4R_e}. \tag{2}$$

Consequently, increasing the operation potential window (U) and the specific capacitance (C), and reducing the equivalent series resistance (R_e) is feasible to improve the energy density and power density of a supercapacitor. The maximum operation potential window for the EDLC supercapacitors depends substantially on the choice of electrolytes such as aqueous electrolyte (0−1 V), organic electrolytes (2.5−2.7 V) and ionic liquids (~4 V) [14]. The specific capacitance for EDLC can be expressed as:

$$C = \frac{\varepsilon_r \varepsilon_0 A}{d}, \tag{3}$$

where ε_r is the relative permittivity of the medium in the EDL, ε_0 is the permittivity of the vacuum, d is the effective thickness of the EDL (charge separation distance), and A is the specific surface area of the electrode [15]. Therefore, the capacitance mainly depends on the formation of EDL and the surface properties of porous electrodes including porosity, shape, dimension, and morphology [16–18]. Comparing with the capacitors which store charge on the electrode surface, the lithium-ion battery which stores charge in the bulk can provide high energy density [19]. In the rechargeable battery, Li ions transfer from the negative electrode to the positive electrode when discharging, and reversely during charge. The transport of Li ions in the porous electrodes and electrolytes, and at the interface between electrode and electrolyte has a direct influence on the electrochemical performance of Li-ion battery, especially for the power density.

Consequently, in order to develop advanced electrical storage devices including both high-energy-density supercapacitors and fast-power-delivery lithium-ion batteries, the design of porous electrode materials requires large surface area to facilitate charge transfer at electrolyte−electrode interface as well as unique porous structures to enhance ion transport from the electrolyte to the electrode surface. The nanomaterials which typically have high surface-to-volume ratio and short diffusion pathways provide an approach to achieve high energy and power density simultaneously [5]. The chemical, structural, and morphological diversity of 0D to 3D nanomaterials including nanoparticles and quantum dots [20−22], nanowires and nanotubes [23,24], graphene [25−27], MXenes [28], metal organic frameworks [29−34], and aerogels [35], allow us to create excellent porous materials for designing advanced energy storage and conversion devices. Developing nanostructured electrode architecture which is favorable for both ion and electron transport is the key to design new porous electrode materials. As a fundamental process, ion transport in nanoscale system presents totally different properties compared with that in bulk electrolyte, which generally appears in confinement between or at the electrode surfaces, having significant consequences in the electrochemical performance. However, understanding the ion transport confined in the nanostructured electrode and the mechanisms and properties at the electrolyte−electrode

interface precisely still remain a challenge, which limits the development of storage energy applications. The ion transport in porous electrode is a complex system that includes diffusion, electrical migration, heat transfer, chemical reaction and electrode process, which may be difficult to access in experiments. Simulation models play a significant role in providing guidance for the development of novel electrolytes, materials and microstructures of porous electrode, in order to satisfy the growing demands in energy density and power density for different promising energy storage applications.

In this paper, we focus on exploring a comprehensive and scientific understanding for the equilibrium structure and dynamic properties of electrolyte in porous electrode. Equilibrium thermodynamic-based simulations, including classical density functional theory (CDFT), classical molecular dynamics (MD), Monte-Carlo (MC), mean-field theory (MFT) and machine learning (ML) methods could be implemented to study the EDL structures and capacitances in different electrode geometries and electrolyte components. Linear non-equilibrium thermodynamic theory is discussed to help us understand non-equilibrium ion transport in porous electrode, involving in Onsager reciprocal relation and linear response. For the dynamic study in porous electrode, molecular modeling like MD can provide detailed information, while continuum modeling solves the system easily and quickly. DDFT shows tremendous potential to be an alternative multiscale method to study the ion transport in porous electrodes and optimize the materials and processes.

2. Equilibrium structure of electrolytes in porous electrodes

2.1. Development of EDL theories

In an electrochemical process, EDL is a very important concept, which describes the distribution of charged species at the electrode−electrolyte interface [36]. As shown in Fig. 1, a model established firstly by Helmholtz considers that the opposite charges are equally distributed on both sides of the interface, which is also the origin of "double layer". Later, the model is improved by Gouy and Chapman jointly, which is called GC model for short. The core of GC model is to introduce a new concept: diffusion layer. At the electrode−electrolyte interface, the charge is strictly distributed on the side of the electrode. On the electrolyte side, due to the interaction between different ions, many charges will diffuse to the bulk solution far away from the interface. However, the charge in GC model is abstracted as a point, which is also a common method in physics. When a large electrode potential is applied, these abstracted "point charges" will be infinitely compressed close to the electrode surface, which is deviated from the actual situation. Therefore, Stern adds a Helmholtz layer to the GC model, considering the ion size of the compact layer in front of the electrode surface, and then get the GCS model. The traditional EDL theory is described by Poisson-Boltzmann (PB) equation, which treats the ions in the electrolyte as point charges. However, for some systems with high
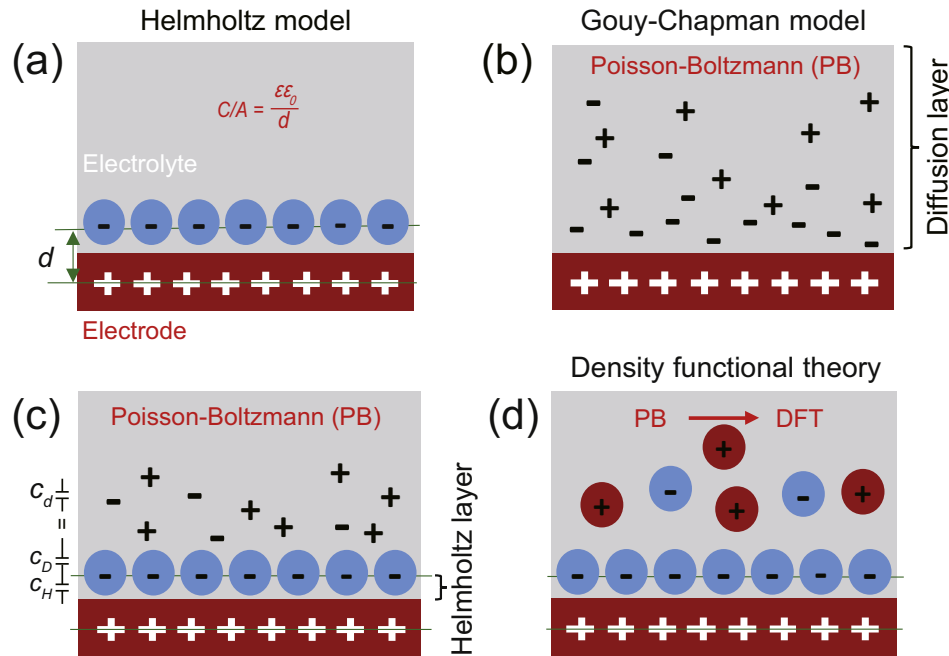
Fig. 1. Development of the EDL model: **(a)** Helmholtz model, **(b)** Gouy-Chapman model, **(c)** Gouy-Chapman-stern model. (d) The Poisson-Boltzmann (PB) theory can be developed by introducing the density functional theory to consider the volume exclusion of solution species in electrolyte.

concentration or strong confinement, the size and interaction force of the ions need to be considered, which can be described by introducing the DFT.

2.2. Classical density functional theory (CDFT)

CDFT is an effective approach to obtain the equilibrium properties of complex liquids [37]. For electrolyte systems, CDFT can be used in the context of both primitive and non-primitive models. In the primitive model, ionic species are represented by charged particles while the solvent is described as a dielectric continuum. A non-primitive model accounts for all components in the electrolyte solution explicitly. For the CDFT calculations, solution species are mostly described by the coarse-grained models [38], in which ionic species are considered as charged hard spheres while solvent molecules are regarded as two tangentially connected spheres of opposite charge. In the model system, the pair potential between any two spheres/segments (i and j) is expressed as:

$$u_{ij}(r') = \begin{cases} \infty, & r' < \dfrac{\sigma_i + \sigma_j}{2} \\ \dfrac{Z_i Z_j e^2}{4\pi\varepsilon_0\varepsilon_r r'}, & r' \ge \dfrac{\sigma_i + \sigma_j}{2} \end{cases}. \quad (4)$$

Here, σ_i is the hard-sphere diameter of particle i, r' is the center-to-center distance, ε_0 is the dielectric constant of the vacuum, and ε_r is the relative permittivity of the solvent, e is the elementary charge.

Given the number densities of ions and solvent molecules in the bulk, the system temperature, the pore size, the pore geometry and the surface electrical potential, the density profiles of cations, anions and the solvent segments inside the

pore can be calculated by minimization of the grand potential. For the electrolyte system containing spherical cations and anions and solvent molecules, the grand potential Ω is calculated by [39].

$$\beta\Omega[\rho_M(R'), \rho_a(r')] = \beta F[\rho_M(R'), \rho_a(r')] +$$
$$\int [\beta\varphi_M(R') - \beta\mu_M]\rho_M(R')dR' + \sum_a \int [\beta\varphi_a(r') - \beta\mu_a]\rho_a(r)dr', \quad (5)$$

where F is the summation of intrinsic Helmholtz energy, $\beta^{-1} = k_B T$, $R' \equiv R'(r_{\delta+}, r_{\delta-})$ describes the positions of two segments in each solvent molecule using two coordinates, here, the superscript of R' is to distinguish it from the gas constant R; r' and r_j specify the positions of ions and solvent segment j, respectively; $\rho_a(r')$ and $\rho_M(R')$ are the total number density of ions and solvent molecules at specific positions, respectively; $\varphi_a(r)$ and $\varphi_M(R')$ respectively stand for the external potential for ions and the total external potential for a solvent molecule, respectively; μ_a and μ_M represent the chemical potential of an ionic species and the solvent, respectively. The number densities of the positive and negative segments of the solvent (δ_+ and δ_-) are given by:

$$\rho_{\delta+}(r_{\delta+}) = \int dR'\delta(r' - r_{\delta+})\rho_M(R'), \quad (6)$$

$$\rho_{\delta-}(r_{\delta-}) = \int dR'\delta(r' - r_{\delta-})\rho_M(R'). \quad (7)$$

An excess contribution resulted from the intermolecular interactions F^{ex}, and an ideal-gas contribution is involved in the intrinsic Helmholtz energy F:

$$\beta F = \int [\ln \rho_M(R') - 1]\rho_M(R')dR' +$$

$$\beta \int V_b(R')\rho_M(R')dR' + \sum_a \int [\ln \rho_a(r') - 1]\rho_a(r')dr' + \beta F^{ex},$$

$$(8)$$

where V_b represents the bonding potential of the solvent molecule. In order to evaluate the Coulomb energy, Poisson equation is used to obtain the mean electrostatic potential Ψ from the ion density distributions:

$$\nabla^2 \Psi = -\frac{e}{\varepsilon_0 \varepsilon_r}\rho_c, \qquad (9)$$

which can be integrated with the boundary value of the operating voltage, here, ρ_c is net ionic density. Based on the overall charge neutrality, the surface charge density Q is obtained. And then the differential capacitance C_d of EDL can be expressed by a derivative of the surface charge density Q with regard to the surface potential.

The EDL structure and capacitance for the electrolyte in different pore geometries can be simulated using CDFT [40–43]. As detailed in previous publications [38,44,45], we can obtain the density profiles of the solution species including anions, cations and solvent molecules inside the pore by minimization of the grand potential. Jiang and Wu used CDFT to calculate the ionic liquid distribution near the surface of the charged plate (Fig. 2a) [46]. Anions are adsorbed on the surface of the positive charged plate to form a compact layer. Because of the negative charge of the compact layer, the

second cation layer is formed, and then the alternating structure of an anion layer and a cation layer is presented. This unique structure is determined by the volume repulsion of the ions and the strong electrostatic interaction between the ions in the ionic liquid, which is difficult to be observed using traditional PB equation. The alternating structure has also been verified by experiments. Different from the EDL of traditional planar electrode, the EDL in the nanochannels of porous materials often exhibit different characteristics. When the two limiting plates are close to the molecular scale, the EDLs of the two solid−liquid interfaces will overlap and interfere with each other, and the structure of the EDL will be changed (Fig. 2b) [47]. To insight the electrostatic screening in ionic liquid, Ma and Lian et al. [48] modeled the surface force using reaction-based CDFT to observe short-range structural decay with exponentially damped oscillation, and long-range exponential force decay (Fig. 2c and d). Fig. 2c shows that the surface force origins from the ideal contribution (Ideal), the steric effect (HS), the Van der Waals attraction (LJ), as well as electrostatic interaction, the long-range surface force decay is primarily shaped by electrostatic interaction, steric effect and reaction equilibrium for different surface charges and bulk concentrations.

As discussed above, CDFT had been used to study the profiles of electrolyte in porous electrode. Furthermore, the CDFT can be used to achieve the rational design of electrode material structure and surface chemical properties. Fig. 3a (top) shows the influence of pore size on the overall integral capacitance of a spherical shell with the inner core radius of 0.5 nm (red line) or a slit pore (black line), and (bottom) the
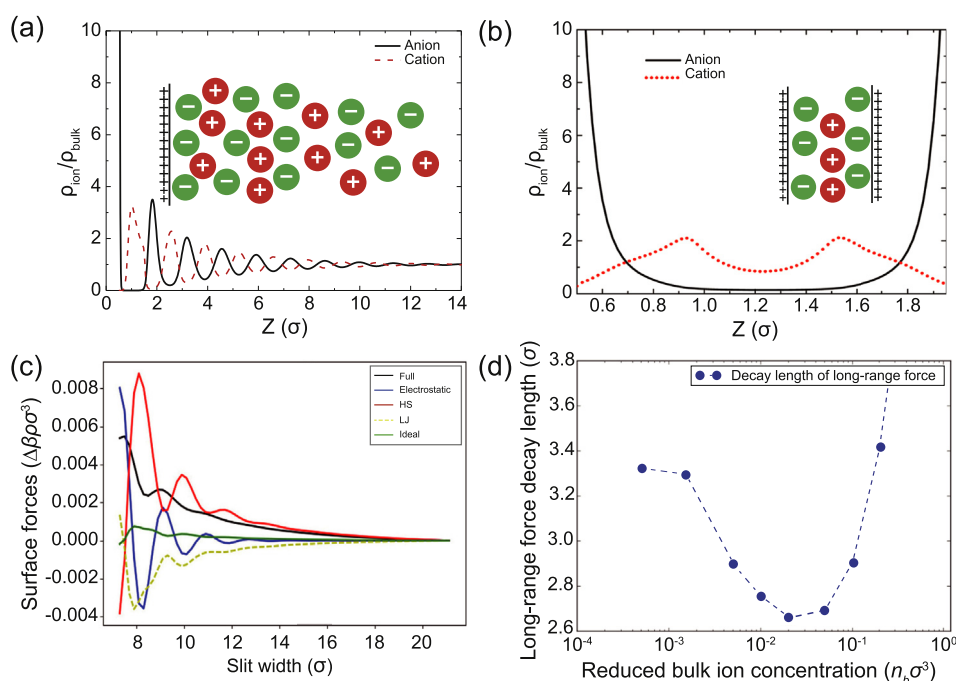

Fig. 2. Ions distribution (ρ_{ion}/ρ_{bulk}) in ionic liquid as a function of location (z) at the charged plate surface [46] **(a)** and between two limiting charged plates **(b)**. Reprinted with permission from Ref. [47]. Copyright (2011) American Chemical Society. **(c)** Surface forces $\Delta\beta P\sigma^3$ arising from various types of interaction as a function of slit width σ. "Full" represents the sum of these surface forces. **(d)** Decay length of long-range force L_s as a function of reduced bulk ion concentration. Reprinted with permission from Ref. [48] for (c−d). Copyright (2019) Elsevier B.V.
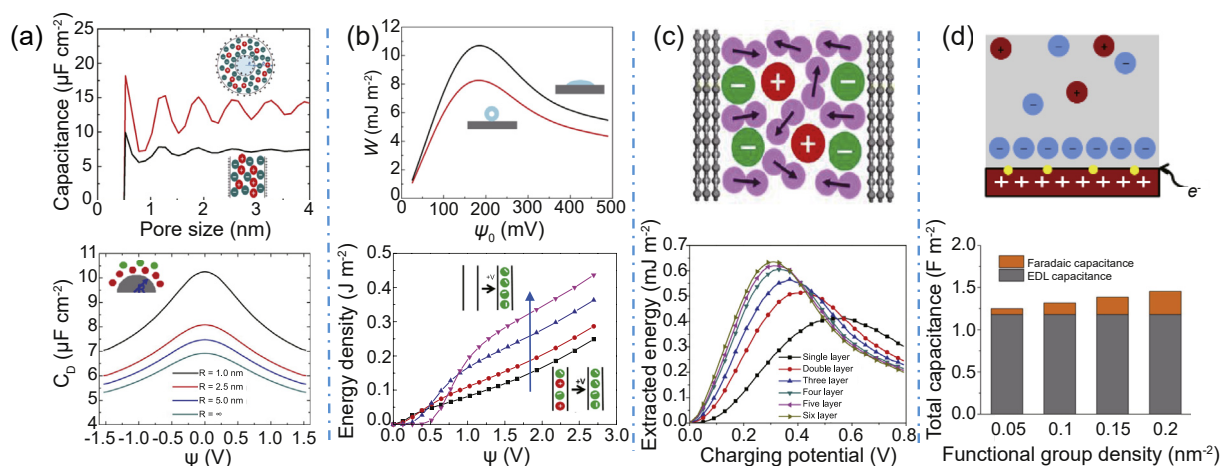
Fig. 3. Rational design of electrode material structure and surface chemical properties, including **(a)** pore structure effects, **(b)** surface properties effects, **(c)** quantum capacitance and **(d)** pseudocapacitance. Reprinted with permission from Ref. [45] for (a). Copyright (2016) American Chemical Society; from Ref. [49,50] for (b). Copyright (2016) IOP Publishing; from Ref. [51] for (c). Copyright (2017) American Chemical Society; from Ref. [52] for (d). Copyright (2020) Elsevier B.V.

curvature effect on differential capacitance of convex interface of a spherical shell with a pore size of 4 nm [45]. The capacitance exhibits the oscillatory dependence on the pore size, while increases significantly as the inner radius decreases. In addition to the pore structure effects, the surface property also plays an important role in the energy stroge capacity (Fig. 3b). At high potentials, an ionophobic pore offers higher storage energy than an ionophilic pore [49,50]. As the stacked graphene layers have been used as porous electrode, Lian et al. [51] studied the contribution of quantum capacitance and EDL capacitance on the capacitance performace of graphene electrode with different number of graphene layers (Fig. 3c). They revealed that the quantum capcacitance played a significant role in extracting energy using single-layer graphene, while the extracted energy was gradually dominated by EDL contribution as the number of graphene layer increases. Considering the presence of Faradaic reactions, Wu and Liu [52] provided a simple molecular model to describe the EDL using the CDFT. They demonstrated that the oxygen functional groups in the electrodes have little influence on the EDL capacitance but can improve the Faradaic capacitance (Fig. 3d).

In addition to the design of porous electrode, the selection and optimization of electrolyte formula with the comprehensive consideration of different factors also can be implemented using CDFT. To identify room-temperature ionic liquids (RTILs) with the largest electrochemical potential windows (EPWs) for optimizing the capacitive performance of EDLCs, Lian et al. [53] investigated the EPWs of 1764 RTILs made from 42 cations and 42 anions (Fig. 4a), which revealed the EPWs of five anions, in the order of $B(CN)_4^- > PF_6^- > BF_4^- > BOB^- > NTf_2^-$ for electrochemical stability, were larger than other anions. Moreover, ionic-liquid mixtures had been explored to achieve larger operation potential window (OPW) and capacitance. The cathodic limit of the mixed system was determined by the maximum of the anions (BF^- and $TFSI^-$), while the anodic limit was up to the

minimum of the cation ($EMIM^+$) (Fig. 4b) [54]. The maximum capacitance was reached when the mole fraction of EMI-BF$_4$ in the RTIL mixture is $x = 0.25$ (Fig. 4c) [55]. For the influence of electrolyte size and shape, Lian et al. studied the capacitance performance of the oligomeric ionic liquid with different chain lengths of oligomeric cations using CDFT (Fig. 4d). When the surface potential is small, the energy density was reduced drastically as the number of monomeric charges in the cation of the oligomeric ionic liquid increases.

2.3. Molecular dynamic (MD) simulations

MD simulation aims to predict the structural and energetic properties of thermodynamic systems by numerically integrating the equations of motion for individual atoms (or coarse-grained representation of molecules) [57,58]. MD simulation has been widely used to observe the EDL structure and specific capacitance of an EDLC in recent years [59]. The results obtained from the MD simulation depend on the molecular model (*viz.*, force fields) used for electrode/electrolyte interactions. When simulating the charged electrodes, constant surface charge method which assigns a constant partial charge directly to each atom on the electrode surface, and constant surface potential method which imposes a constant potential drop between the two electrodes are often employed. The simulation results obtained from the constant charge method match well with the experimental results in both EDL structures and capacitance [60], but ignores the possible fluctuation of surface charges induced by electrolytes. The constant potential method can be used to overcome the drawback, which can redistribute the surface charges on the electrode atoms over the course of simulation to meet the condition minimizing the electrostatic energy of the system [61,62]. A number of researchers have made a comparison between the two methods for simulating supercapacitors. Merlet et al. found that for the planar surface, both two methods showed quite similar ionic density distributions at a low potential
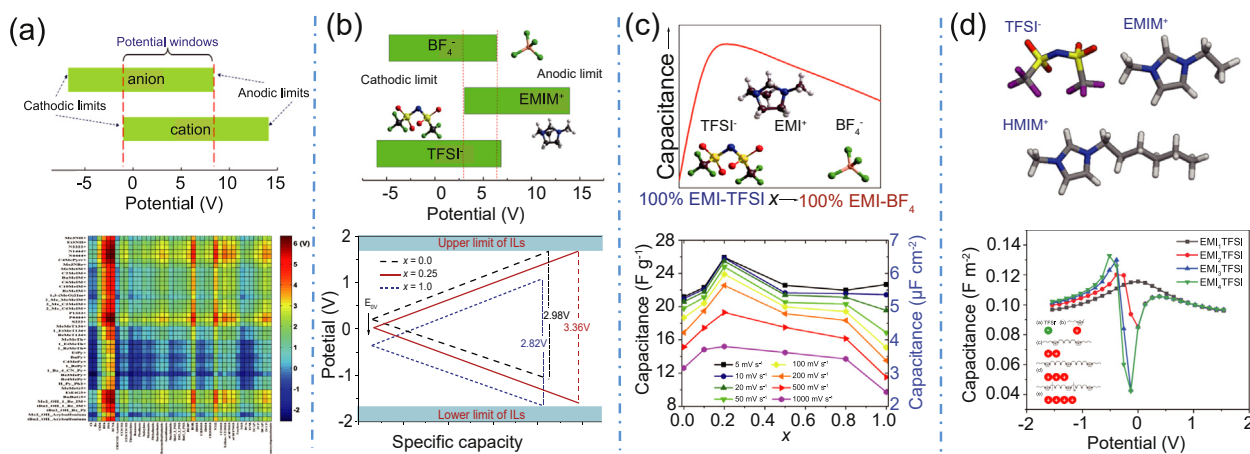
Fig. 4. Comprehensive consideration of different factors to achieve the selection and optimization of electrolyte formula, such as **(a)** fast screening of RTIL electrolytes, **(b)** electrolyte mixture to enhance OPW, **(c)** electrolyte mixture to enhance the capacitance, **(d)** electrolyte size and shape effects. Reprinted with permission from Ref. [53] for (a). Copyright (2019) John Wiley and Sons; from Ref. [54] for (b). Copyright (2018) American Chemical Society; from Ref. [55] for (c). Copyright (2016) American Chemical Society; from Ref. [56] for (d). Copyright (2018) American Chemical Society.

difference [63], while presented large structural differences for EDL at a high potential drop: higher peaks of counter-ion or co-ion distributions near the surface were obtained from the constant potential method compared with those from the constant charge method (Fig. 5a). The variable surface charge on the constant potential electrode had significant consequences for such differences, which responds to local fluctuations of the charge density in electrolyte and creates more favorable electrostatic interactions (Fig. 5b) [64].

In addition to the polarizability of electrodes, it is crucial to utilize appropriate force fields for the electrolyte in order to obtain realistic structural and dynamic information from MD simulations. For room-temperature ionic liquids (RTILs), various classical force fields have been developed involving coarse-grained models [65,66], united-atom models [67–69], and all-atom models [70]. The coarse-grained force fields can significantly reduce the computational cost due to the simplified molecule, while the all-atom force fields can present a detailed representation of the electrostatic interactions and molecular configurations for the EDL.

2.4. Grand Canonical Monte Carlo (GCMC)

Constant voltage GCMC is also a practical method to solve the thermodynamic equilibrium issues for the electrode/electrolyte interface, which is developed by Kiyohara et al. for a two-electrode system with planar electrodes and the hard-sphere ion model [71,72]. The constant voltage is implemented with electrode charge balance and exchange. The induced charge and capacitance at a specified voltage difference of the two electrodes are obtained after reaching the thermodynamic equilibrium.

Similar to CDFT and classical MD calculations, the asymmetric charging behavior caused by asymmetric ion sizes was successfully simulated through the constant voltage GCMC [71]. The obtained density profile is more detailed than that from the conventional double layer theory (Fig. 1). The GCMC work by Kiyohara also captures the ionic response in an ideal nanochannel (including both mono- and multi-channel) at constant electrode voltage [72]. However, the electrode and electrolyte ions are highly simplified, and the
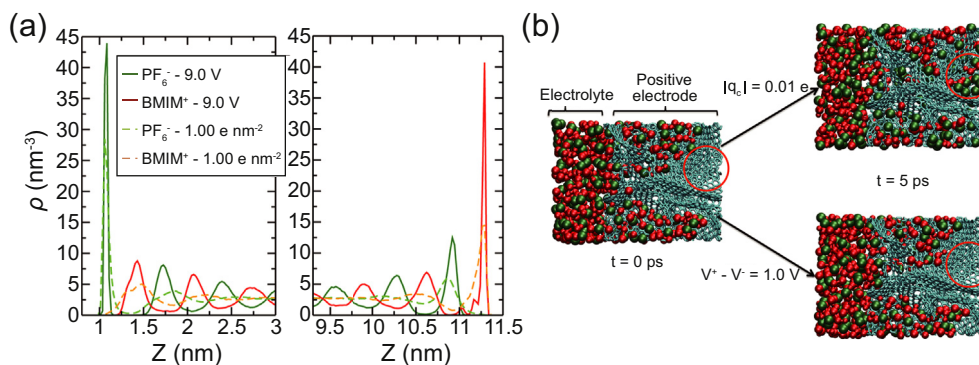

Fig. 5. **(a)** Profiles of the ionic density for the simulations when the constant potential of 9.0 V or the constant charge of 1 e nm^{-2} was applied. **(b)** Evolution of the positive electrode inside for the simulations using the constant charge method or constant potential method. Reprinted with permission from Ref. [63]. Copyright (2013) American Chemical Society.

explicit solvent effect is not included in this work. Bhatia et al. applied the constant voltage GCMC to atomically modeled flat carbon electrodes as well as porous carbon electrodes [73,74]. The oscillating behavior of capacitance for an ionic liquid electrolyte confined in the silt nanopore obtained from the constant voltage GCMC was similar to the results from the CDFT and MD simulations.

2.5. Mean-field theory (MFT)

With approximations to describe steric effects and electrostatic interactions, a mean-field theory (MFT) can be used to capture the "bell" or "camel" shaped differential capacitance (C_d) curves which are often investigated in experiment [75]. The high-voltage behavior can be attributed to the "lattice saturation" or "crowding" due to excluded volume effects, which is not captured in the GC model that serves solution species as points [76,77].

RTILs are typically composed of organic ions that are asymmetric for different volumes of anions and cations, leading to asymmetric capacitance and voltage curves. Kornyshev et al. developed a semi-empirical formulism by modifying the differential capacitance for symmetric ions to study the asymmetric effect [78]. However, MFT is difficult to take the correlation effects and the inhomogeneous properties of porous electrodes into consideration.

2.6. Data based models and machine learning (ML)

Recently, machine learning (ML) methods have been developed to study and predict the capacitance of carbon-based supercapacitors, in which the published experimental data is used to train ML models to determine the relative importance of these electrode variables [79–81]. The data-based method can be used as an alternative approach to explore many practical problems such as the influences of operation variables on the real-time performance of electrochemical capacitors. Provided that sufficient training data are variable, ML methods allow us to establish useful correlations between materials properties and their performance without evoking the physical details.

Linear regression (LR) describes the relationship between experimental results and operation parameters with a linear regression equation, which is easy to interpret, and fast in making predictions, but has low predictive accuracy. In contrast, Lasso is a regression analysis method that performs both variable selection and regularization in order to enhance the prediction accuracy and interpretability of the statistical models [82]. Support vector regression (SVR) is also an excellent regression technique for regression and time series prediction application, categorizing the input data using separating lines or planes [83]. Artificial neural network (ANN) have been used by Zhu et al. to study the influence of five parameters (N-doping level, pore size, Raman I_D/I_G ratio, potential window and specific surface area) on the capacitance of supercapacitors [84], which is compared with two other ML models (Lasso and LR), showing higher accuracy, but cannot

reveal the influence of each variable separately. Deep learning networks depend on layers of the ANNs, which are often regarded as a black box, and the outputs are difficult to correlate with physical phenomena. Therefore, ML algorithms are developed to make the outputs more explicable [85]. Multilayer perceptron (MLP) is a widely used ANN model, including an input layer, hidden layers and an output layer, and each layer consists of nodes connected with a certain weight to all nodes in the next layer [86]. Su et al. [87] studied the influence of porous carbon materials and potential windows on the EDL capacitance by using four ML models. They collected 121 sets of carbon-based supercapacitors with seven variables reported from different papers as the input of different ML models (Fig. 6a–h). Based on these selected data and variables, four different ML methods were used to predict the capacitance (Fig. 6i); then, a comparison between the predicted capacitance and real experimental capacitance, and among these methods, MLP shows best performance (Fig. 6j). In addition, the prediction of the solvent effect on the EDL capacitances (Fig. 6k) can be also implemented using the ML methods with the same sequential approach [88].

3. Nonequilibrium transport of electrolytes in porous electrode

The transport processes in porous electrode, including diffusion, migration, heat transfer, fluid flow, chemical reaction and electrode process, are highly coupled in the energy storage and conversion system, which are irreversible processes that change over time and from nonequilibrium to equilibrium [89,90]. Here, different methods which can be used to study these nonequilibrium processes will be discussed. The experimental methods for corresponding study of electrolytes and porous electrodes are limited by the development of advanced experimental equipment and micro measurement technology. According to the linear nonequilibrium thermodynamics, the coupling effects between different thermodynamic forces on the ion transport in the electrochemical system can be described by the non-diagonal terms of response matrix [91]. Analytical solutions focus on solving the phenomenological coefficient matrix by mathematical derivation to require the non-diagonal terms of the matrix to describe the interaction of different thermodynamic forces [92]. Molecular modeling has been widely used to study some special transport phenomena, such as charging dynamic, electrokinetic phenomena and thermoelectric effect, which can provide detailed information about the transport processes but requires extensive computational effort. Continuum modeling is an effective approach to explore dynamic properties in the electrochemical system quickly, which is limited by the dilute solution theory that will be broken in molecular scale or at high applied potential [93]. Therefore, DDFT can provide an alternative method for studying these transport phenomena quickly and accurately with the consideration of steric effect and other interaction, which is expected to be a link between the MD and continuum models.
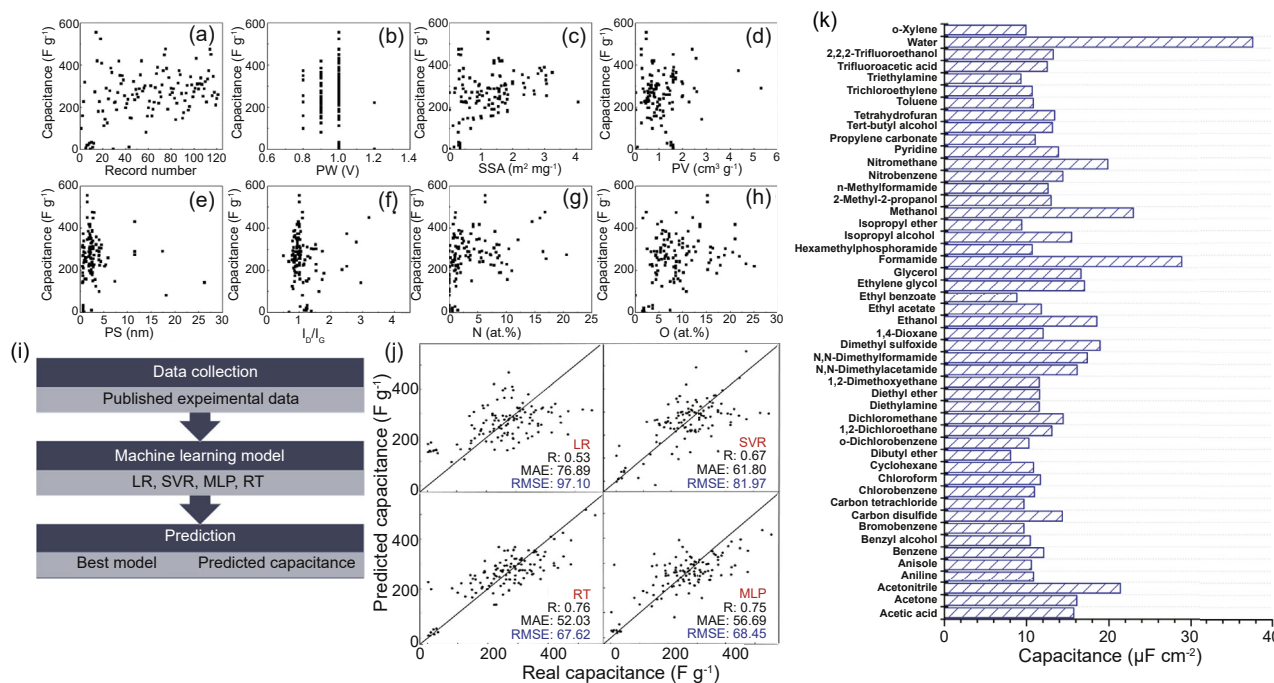
Fig. 6. Input data with different variables, 121 sets of capacitances for different carbon-based electrodes. The relationship between the (a) capacitance and (b) potential window, (c) specific surface area, (d) pore volume, (e) pore size, (f) ratio of I_D/I_G, (g) N-doping percentage, and (h) O-doping percentage. (i) EDL capacitance was predicted by using ML models with the sequential approach. (j) Statistical performance of each ML model by comparing the predicted capacitance from ML models (y-axis) and the real experimental capacitance (x-axis) [87]. (k) Prediction of the solvent effect on the EDL capacitances from the MLP method. Reprinted with permission from Ref. [88]. Copyright (2019) Elsevier B.V.

3.1. Experimental observation

As the development of advanced characterization methods, some experimental techniques are used to characterize EDL for revealing the underlying physics and validating the simulation results and theoretical prediction. An important tool to study the microscopic dynamics inside porous electrode is Quasi-Elastic Neutron Scattering (QENS) [94,95], which involves the time scale of ps and ns for ion diffusion. Some dynamic electrochemical processes including intercalation, potential-dependent ion transport, and local electrochemical reactivity can be explored by the Electrochemical Strain Microscopy (ESM) [96–98]. X-ray reflectivity is also an effective approach to probe the structure of electrolyte at the solid/liquid interface for the flat substrate [99–101]. A direct measurement of the EDL structure can be implemented by Scanning Probe Microscopy (SPM) through the Atomic Force Microscopy (AFM) tip approaching the surface [102–104]. Moreover, Sum Frequency Generation (SFG) [105] and Second Harmonic Generation (SHG) [106] could provide some structural information of the interface for carbon electrodes. Nuclear Magnetic Resonance (NMR) [107,108] is also applied to observe the ion structure at interface and provide the information of ion dynamics.

Lis et al. firstly reported the influence of fluid flow on the interfacial reaction and the structure of EDL in experiment (Fig. 7a) [109]. The microfluidics and surface-specific SFG spectroscopy were combined to demonstrate that fluid flow results in a reversible realignment of the interfacial water

molecules and a modification of the surface charge at immersed surfaces (Fig. 7b−d). Two different temperature-dependent experiments were implemented by Janssen et al. to study the temperature effects in the EDLCs involving porous carbon electrodes (Fig. 8a) [110], which revealed a charge decrease when increasing temperature at a fixed voltage in the Coulometric experiment, and the production of both reversible heat and irreversible Joule heat in the calorimetric experiment (Fig. 8b).

Although various experimental techniques have been discussed above, the observation of non-equilibrium properties in porous materials using experimental methods still remains a challenge. On the one hand, they can only infer some non-equilibrium properties of porous electrode or solid−liquid interface based on some macroscopic properties. On the other hand, they pay attention to the influence of a single driving force rather than a coupling of different driving forces; the latter is widespread in practical research. Consequently, theoretical and simulation studies are necessary for explaining the non-equilibrium phenomena in the experiment, simultaneously understanding the underlying physics in combination with the experiment.

3.2. Linear nonequilibrium thermodynamics

3.2.1. Linear relation and Onsager matrix

Similar to the function of equilibrium thermodynamics, nonequilibrium thermodynamics reveals some valuable universal connections between different transport properties [91].
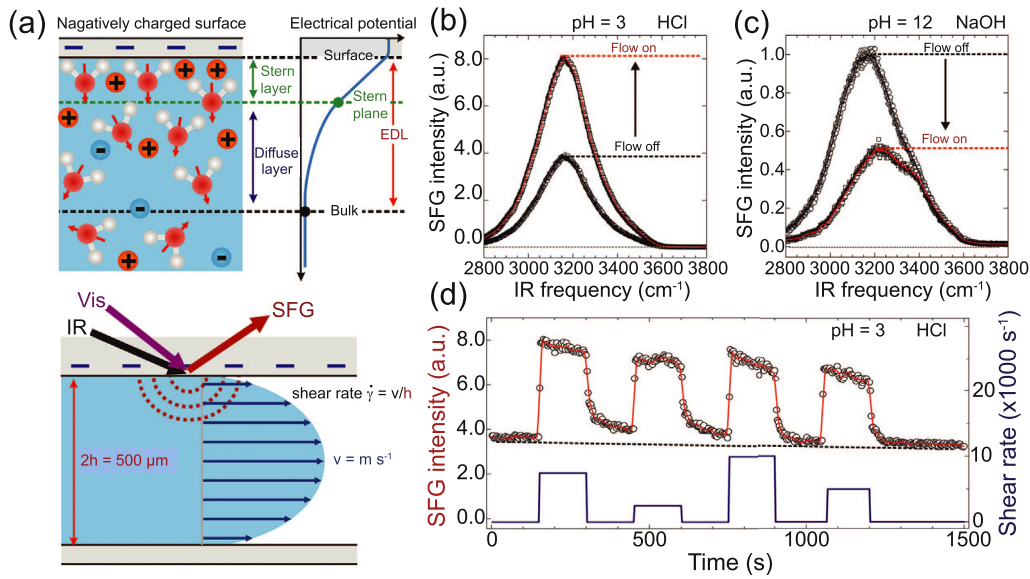
Fig. 7. (a) (**Top**) The profiles of electrical potential and solution species near the negatively charged interface; (**Bottom**) Schematic of the experiment method for studying the influence of fluid flow on the structure of solid−liquid interface based on Vis, IR and SFG. SFG spectrum of the solid−liquid interface at (**b**) pH = 3 and (**c**) pH = 12 with flow (red) and static (black) conditions. (**d**) Time dependence of SFG intensity (black circles) of the solid−liquid interface at pH = 3 under multiple flow on−off cycles (blue curve). Reprinted with permission from Ref. [109]. Copyright (2014) the American Association for the Advancement of Science.
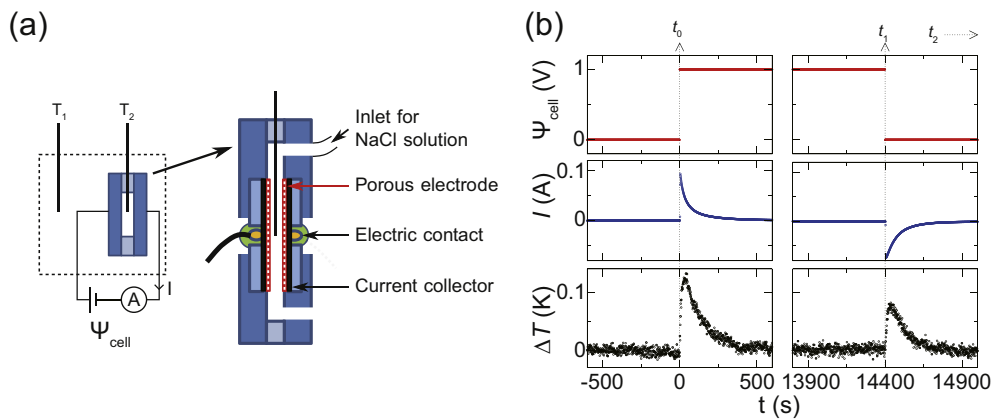

Fig. 8. (**a**) Schematic representation of an experimental method to measure temperature and current for the charging and discharging processes of porous electrodes in NaCl solution. (**b**) The current and temperature response in the calorimetric experiment when the system was applied with a step voltage. Reprinted with permission from Ref. [110]. Copyright (2017) American Physical Society.

Based on the theory of the second law of thermodynamics, we can describe the change of the system from the perspective of entropy dS, and for isolated system:

$$dS = dS_g \geq 0, \tag{10}$$

where S_g is generation entropy. For non-isolated systems, the exchange of energy or matter with the outside environment should be considered:

$$dS = dS_g + dS_{ex} = dS_g + \frac{\delta T}{T}, \tag{11}$$

where S_{ex} is exchange entropy, T is temperature of system. The nonequilibrium thermodynamics studies the irreversible process inside the system, so the exchange of energy and

substance between the system and the environment can be regarded as a reversible process. Whether the system is in equilibrium or not, the irreversible process can be described by the entropy change inside the system, which is applicable to isolated system, closed system and open system. Consider the rate of entropy generation due to the irreversible process in the system, i.e. entropy growth rate:

$$\frac{dS_g}{dt} = \dot{S}_g = \sum_{i=1}^{n} J_i X_i \geq 0. \tag{12}$$

Here, J_i and X_i are thermodynamic flux and corresponding force respectively of the transport process i. Furthermore, the linear relation equation between thermodynamic fluxes and forces in various irreversible processes can be derived, namely, the linear phenomenological equation:

$$J_i = \sum_{k=1}^{n} L_{ik} X_k, \tag{13}$$

where L_{ik} is the phenomenological coefficient. In addition to the entropy generation rate and linear phenomenological equation, Onsager's theorem is also the basis of the thermodynamics of irreversible process. It further proves the reciprocal relationship ($L_{ij} = L_{ji}$) between the non-diagonal terms in the phenomenological coefficient matrix below, so that people can get the possible universal relationship among the characteristics of various irreversible processes:

$$\begin{bmatrix} J_1 \\ J_2 \\ J_3 \\ J_4 \\ J_5 \end{bmatrix} = \begin{bmatrix} L_{11} & L_{12} & L_{13} & L_{14} & L_{15} \\ L_{21} & L_{22} & L_{23} & L_{24} & L_{25} \\ L_{31} & L_{32} & L_{33} & L_{34} & L_{35} \\ L_{41} & L_{42} & L_{43} & L_{44} & L_{45} \\ L_{51} & L_{52} & L_{53} & L_{54} & L_{55} \end{bmatrix} \begin{bmatrix} \nabla u \\ \nabla \phi \\ \nabla P \\ \nabla T \\ A \end{bmatrix}. \tag{14}$$

In a word, linear nonequilibrium thermodynamics provides not only a macroscopic phenomenological framework for different transfer phenomena such as diffusion, heat transfer and momentum transfer, but also a basis for the study of their mutual relations and influences. We hope these theories for nonequilibrium thermodynamics help us understand nonequilibrium ion transport in porous electrode with considering the coupled effect of diffusion, electrical migration, heat transfer, fluid flow and chemical reaction (Table 1).

3.2.2. Analytical methods

In order to study nonequilibrium ion transport in an electrochemical system accurately, we need to solve the 5×5 Onsager matrix considering the interplay between diffusion, electrical migration, heat transfer, pressure drop and chemical reaction, which is difficult for the mathematical derivation. Currently, the 3×3 response matrix involving the difference in pressure, electric potential and salt concentration have been solved for charged nanopores and nanochannels:

$$\begin{bmatrix} Q \\ I \\ J \end{bmatrix} = \begin{bmatrix} L_{11} & L_{12} & L_{13} \\ L_{21} & L_{22} & L_{23} \\ L_{31} & L_{32} & L_{33} \end{bmatrix} \times \begin{bmatrix} \nabla P \\ \nabla V \\ \nabla \mu \end{bmatrix}. \tag{15}$$

which relates the fluxes, Q, I and J, to corresponding driving forces, ∇P, ∇V and $\nabla \mu$. Peters and van Roij [92] studied the nonlinear electrokinetic response of the charged nanopores using a capillary pore model which assumes local quasi-equilibrium based on a semi-analytical method (Fig. 9a). Due to the local linear response results from the assumption of

local quasi-equilibrium, the equivalence and Onsager reciprocal relations have been demonstrated in all symmetric force-flux frameworks. The response matrix, which relates the fluxes, u_x, $j_{ions,x}$ and $j_{ch,x}$, and corresponding driving forces, $-\partial_x p_{t,v}$, $-\partial_x \mu_v$, and $-\partial_x \phi_v$, can be expressed as [92]:

$$\left(u_x(r), j_{ions,x}(r), j_{ch,x}(r)\right)^t = \begin{pmatrix} L'_{11} & L'_{12} & L'_{13} \\ L'_{21} & L'_{22} & L'_{23} \\ L'_{31} & L'_{32} & L'_{33} \end{pmatrix} \left(-\frac{\partial p_{t,v}}{\partial x}, -\frac{\partial \mu_v}{\partial x}, -\frac{\partial \phi_v}{\partial x}\right)^t, \tag{16}$$

where,

$$L'_{11} = +\frac{1}{4\alpha}(1 - r^2),$$

$$L'_{12} = -\frac{2c_v}{\alpha}\left(\ln r \int_0^r r_1 \cosh \psi(r_1) dr_1 + \int_0^r r_1 \ln r_1 \cosh \psi(r_1) dr_1\right),$$

$$L'_{13} = +\frac{2}{\alpha}\lambda_{ref}^2(\psi(r) - \psi_w),$$

$$L'_{21} = +\frac{c_v}{2\alpha}(1 - r^2)\cosh\psi(r),$$

$$L'_{22} = -\frac{4c_v}{2\alpha}\cosh\psi(r)\left(c_v\left(\ln r \int_0^r r_1 \cosh\psi(r_1)dr_1 + \int_0^r r_1 \ln r_1 \cosh\psi(r_1)dr_1\right) - \frac{\alpha}{2}\right),$$

$$L'_{23} = +\frac{4c_v}{2\alpha}\left(\cosh\psi(r)\lambda_{ref}^2(\psi(r) - \psi_w) - \frac{\alpha}{2}\sinh\psi(r)\right),$$

$$L'_{31} = -\frac{c_v}{2\alpha}(1 - r^2)\sinh\psi(r),$$

$$L'_{32} = +\frac{4c_v}{2\alpha}\sinh\psi(r)\left(c_v\left(\ln r \int_0^r r_1 \cosh\psi(r_1)dr_1 + \int_0^r r_1 \ln r_1 \cosh\psi(r_1)dr_1\right) - \frac{\alpha}{2}\right),$$

Table 1
Linear phenomenological relations between different thermodynamic fluxes and forces.

| Thermodynamic force X_k	Flow J_k	Linear rule	Phenomenological coefficient L_{ij}
Temperature gradient ∇T	J_q	Fourier law $J_q = -K\nabla T$	Thermal conductivity k
Chemical potential gradient ∇u	J_w	Fick law $J_w = -D\nabla u$	Diffusion coefficient D
Electrical potential gradient $\nabla \varphi$	J_e	Ohm law $J_e = \Lambda\nabla\varphi$	Conductivity Λ
Pressure gradient ∇P	J_f	Newton law $J_f = \eta\frac{dv}{dz}$	Viscosity η
Chemical affinity A	J_e	Chemical reaction law $J_c = lA$	Rate constant l
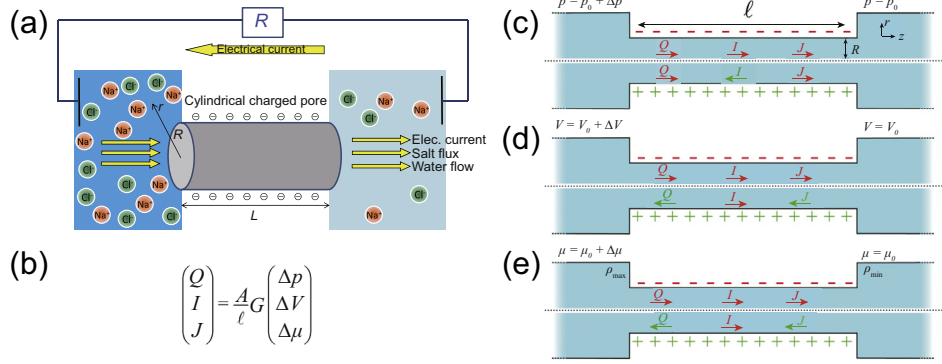
Fig. 9. **(a)** Schematic of a charged nanopore model under the influence of pressure, potential and concentration gradient. Reprinted with permission from Ref. [92]. Copyright (2016) American Chemical Society. **(b)** A conductivity matrix G is used to describe the relation between the driving forces and generated fluxes. **(c)** Pressure difference Δp, **(d)** electrostatic potential difference ΔV or **(e)** chemical potential difference $\Delta \mu$ are imposed across a nanochannel for a typical electrokinetic system. Reprinted with permission from Ref. [111] for (b-e). Copyright (2020) American Chemical Society.

$$L_{33}' = -\frac{4c_v}{2\alpha}\left(\sinh\psi(r)\lambda_{ref}^2(\psi(r)-\psi_w) - \frac{\alpha}{2}\cosh\psi(r)\right). \quad (17)$$

Here, we can assume local equilibrium in the r direction, "radial potential" $\psi(r)$ is obtained equilibrium PB model, ψ_w is the value of potential ψ at the pore wall, $\phi_v(x)$ is virtual potential which accounts for axial gradients in potential (along the length of the pore), μ_v is virtual chemical potential; $c_v(x)$ is virtual concentration, $p_{t,v}(x)$ is virtual pressure; α is the dimensionless viscosity parameter, λ_{ref} is a dimensionless reference Debye length in units of the cylinder radius.

Similarly, considering the gradient of pressure, electric potential and salt concentration (Fig. 9c−e), Werkhoven [111] used the 3×3 Onsager matrix **L** relating the fluxes to the driving forces to describe the electrokinetic response of nanofluidic devices. The local linear-response Onsager matrix L is extended to a global linear-response conductivity matrix G (Fig. 9b). The non-zero off-diagonal terms of G, which highlight the interaction of different driving forces, can describe the unique transport properties of nanofluidic devices.

3.3. Dynamic research using molecular modeling

As discussed above, the MD simulation can describe the EDL structure and optimize the capacitance. Furthermore, it has been extensively used to investigate the transport laws and mechanisms in nanoscale [112−115]. To improve the power density of supercapacitors with ionic liquids and nanoporous electrodes, MD simulations were applied to study the charging and discharging behaviors in nanopores. Kondrat et al. [116] revealed a square root growth of the accumulated charge in slit pores (Fig. 10a, **top**), and the charging of ionophilic pores was a diffusive process, often accompanied by overfilling followed by de-filling. In their study, the charging of nanopores nonmonotonically with time agreed with that from the MFT predictions. The ionophobic pores can accelerate charging by an order of magnitude (Fig. 10a, **bottom**), where a transition from self-diffusion to collective Fickian diffusion was observed. Furthermore, Breitsprecher et al. [117] used MD simulations to study the charge transport in subnanometer pores using step-voltage method. They demonstrated that

counter-ion adsorption exhibits three regimes, including the linear growth, square-root and exponential diffusive regimes (Fig. 10b, **top**). They revealed that a slow charging behavior during the fast-linear stage was caused by the compression of absorbed counter-ions for the in-pore ionic liquid, and thus resulting in a crowded neutral phase inside the pores and strong co-ion trapping; therefore, the slow charging can be accelerated by slowing down the charging process through incremental increase of voltage (Fig. 10b, **bottom**). Recently, Mo et al. [118] studied the charging dynamic of subnanometer pores, their results showed a non-monotonic relation between the charging rate and pore size, and the charging process could be accelerated in some pores due to the transition of in-pore ion structure (Fig. 10c).

An approach of combining MD simulation and linear nonequilibrium thermodynamics has been developed. The thermodynamic flux can be obtained under different thermodynamic forces using the MD simulation, and then the off-diagonal terms of the Onsager matrix are calculated to describe the interaction between two thermodynamic forces. Based on the Onsager's reciprocal relation and linear response, Fu et al. [119] used the MD simulations to investigate the thermoelectric response of salt solution in the charged silt pores (Fig. 11a and b). The off-diagonal terms of the response matrix (M_{21} and M_{21}) can describe the thermoelectric response of the system under the influence of electric potential gradient $-\nabla U$ and temperature gradient $-\nabla T$:

$$\begin{bmatrix} j_e \\ j_h \end{bmatrix} = \begin{bmatrix} \sigma & M_{12} \\ M_{21} & \kappa T \end{bmatrix} \times \begin{bmatrix} -\nabla U \\ -\dfrac{\nabla T}{T} \end{bmatrix}, \quad (18)$$

where, j_e is the electric current density, j_h is the heat flux density, σ and κ are the electrical and thermal conductivities of the system. According to Onsager reciprocal relation, thermoelectric coefficient is expressed as $M_{TE} = M_{21} = j_h/E_x$, $E_x = -\nabla U$. Yoshida et al. [120] used a non-equilibrium MD (NEMD) method to study diffusio-osmosis by applying an external driving force to every particle (Fig. 11c and d). Based on the linear response theory, influences of chemical potential
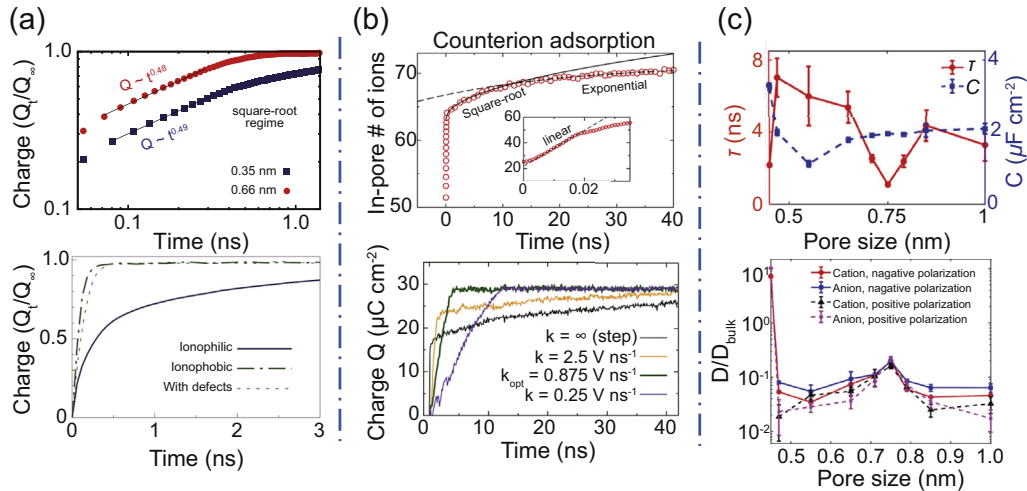
Fig. 10. Different approaches to accelerate the charging dynamic of the supercapacitors with ionic liquids and nanoporous electrodes, such as **(a)** considering the ionophobic pores, **(b)** applying a slow voltage sweep and **(c)** changing the pore size. Reprinted with permission from Ref. [116] for (a). Copyright (2014) Springer Nature; from Ref. [117] for (b). Copyright (2018) American Chemical Society; from Ref. [118] for (c). Copyright (2020) American Chemical Society.

gradient $\nabla_x \mu$ and pressure gradient $\nabla_x P$ on both solvent flow and solute are expressed in the transport matrix:

$$\begin{bmatrix} Q_t \\ J_S - c_\infty^* \end{bmatrix} = \begin{bmatrix} M^{QQ} & M^{QJ} \\ M^{JQ} & M^{JJ} \end{bmatrix} \times \begin{bmatrix} -\nabla_x P \\ -\nabla_x \mu \end{bmatrix}. \quad (19)$$

where Q_t and $J_S - c_\infty^*$ are the total (volume) flux and the excess solute flux, respectively. The off-diagonal terms of the response matrix $M^{QJ} = M^{JQ}$ due to the Onsager reciprocal relation, which are regarded as the transport coefficients of the diffusio-osmotic process relating the generated fluxes with the external field.

3.4. Multiphysics coupled PNP equations

The continuum modeling provides an effective approach to study the ion transport in porous electrode. Microstructure models of the porous materials could be constructed to study
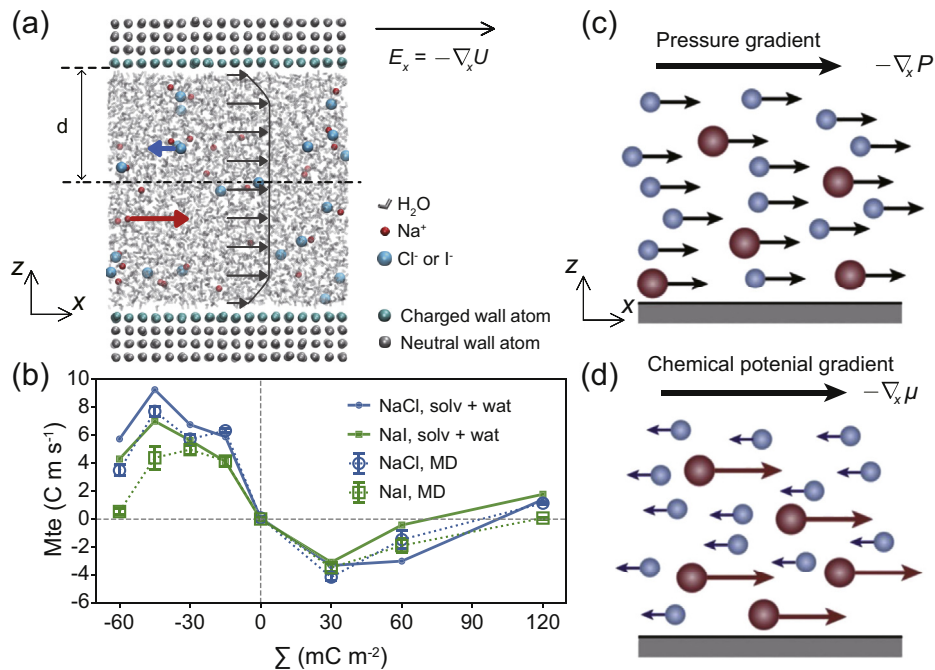

Fig. 11. **(a)** Schematic representation of the MD simulation system for thermoelectrical response. **(b)** Thermoelectrical coefficient M_{TE} as a function of surface charge Σ with a comparison between NaCl and NaI solutions. Reprinted with permission from Ref. [119] for (a,b). Copyright (2019) American Physical Society. Schematic of the NEMD method for studying diffusio-osmosis by imposing **(c)** a pressure gradient or **(d)** a chemical potential gradient to each particle. Reprinted with permission from Ref. [120] for (c,d). Copyright (2017) AIP Publishing.

the properties of the microscale ion transport. The model system can be implemented by solving the coupled partial differential equations with the finite element method.

The Poisson-Nernst-Planck (PNP) equations [121–123], which describe both the mass transport of solution species and the electrical potential distribution in electrolyte, can be used to study different non-equilibrium processes coupled with other transport equations, such as Navier−Stokes (NS) equation, heat equation and Butler-Volmer (BV) equation [124]. The full set of PNP Equations can be expressed as Eqs. (9), (20) and (21):

$$\partial_t \rho_i = -\partial_x J_i \,, \tag{20}$$

$$J_i = -D_i \left(\partial_x \rho_i + \frac{z_i e \rho_i}{k_B T} \partial_x \Psi \right) \tag{21}$$

where ρ_i and J_i are the number density and ionic flux of the ith ion species respectively, z_i is the ith ion algebraic valence, D_i is the diffusion constants, k_B is Boltzmann constant, T is temperature; Ψ is electrical potential which can be described by using Eq. (9). Based on the PNP and NS equations, Tao et al. [125] used a simple layered membrane model to study the influence of different interlayer spacing distributions on the ion transport in graphene-based membranes (Fig. 12a). For an incompressible fluid, the fluid movement is governed by the continuity and the Navier−Stokes equations:

$$\nabla \cdot u = 0, \tag{22}$$

$$\varrho \frac{\partial u}{\partial t} + \varrho (u \cdot \nabla) = -\nabla P + \eta \nabla^2 u - e \sum_i z_i \rho_i \nabla \Psi, \tag{23}$$

where u is the velocity of the solvent, ϱ is the mass density, η is the dynamic fluid viscosity, P is the applied external pressure force. The different interlayer spacing distributions can be controlled by the offset angle of the middle nanosheet of the layered membrane model. The suitable interlayer spacing distribution for the layered membrane was favorable for increasing the EDL overlapping and decreasing spatial confinement, and thus having a positive influence on the ion selectivity and water permeation. In addition to the above-mentioned experimental approach and MD method, the thermoelectric response in porous electrode also can be explored using the multi-physics coupling method, which is governed by Poisson, Nernst−Planck and heat (PNPh) equations, as shown in Eqs. (9), (20), (24) and (25) [126–129]:

$$J_i = -D_i \left(\partial_x \rho_i + \frac{z_i e \rho_i}{k_B T} \partial_x \Psi + \frac{\rho_i Q_i^*}{k_B T^2} \partial_x T \right) , \tag{24}$$

$$\partial_t T = a \partial_x^2 T - \frac{e}{\varrho c_p} (J_+ - J_-) \partial_x \Psi , \tag{25}$$

where Q_i^* is single-ion heats of transport, κ_θ and c_p are the specific thermal conductivity and the heat capacity respectively, $a = \kappa_\theta / (\varrho c_p)$. Janssen used the PNPh equations to study the reversible heating in EDLCs (Fig. 12b, **top**), and gave a deep understanding of reversible temperature variations
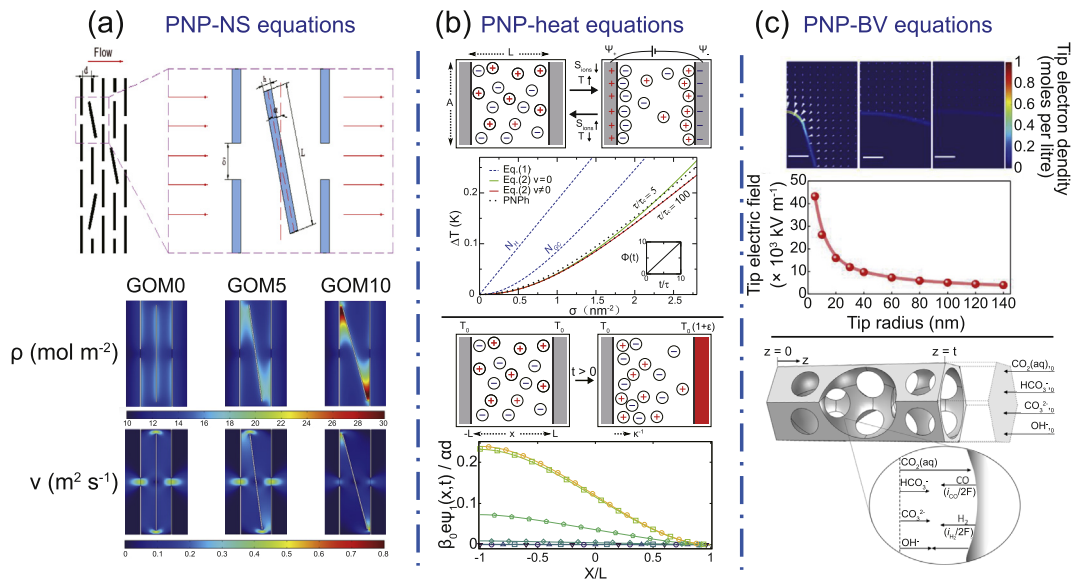

Fig. 12. (a) (**Top**) schematic of the layered membrane model. The interlayer spacing distribution was described by an offset angle α of the middle sheet (**bottom**) The average flux of counter-ion through the layered membrane model as a function of the offset angle α with different driven pressure ΔP. Reprinted with permission from Ref. [125]. Copyright (2020) Elsevier B.V. (b) (**Top**) Schematic of ionic entropy change under charging or discharging, leading to a response of the temperature T of electrolyte. Reprinted with permission from Ref. [129]. Copyright (2017) American Physical Society. (**bottom**) Sketch of the change of ion distribution when one flat electrode was imposed with a temperature quench. Reprinted with permission from Ref. [127]. Copyright (2019) American Physical Society. (c) Influence of electrode structure on the electrochemical reduction of CO_2 (**Top**) Free electron density distribution on the surface of electrodes is shown as a color map. The tip radius of the structure in each panel is 5 nm (left), 60 nm (middle) and 140 nm (right). And electrostatic field intensity at the electrode tip increases as the tip radius decreases. Reprinted with permission from Ref. [93]. Copyright (2016) Springer Nature. (**bottom**) Illustration of the mass transport model for electrochemical reduction of CO_2 on Ag−IO. Reprinted with permission from Ref. [132]. Copyright (2019) Royal Society of Chemistry.
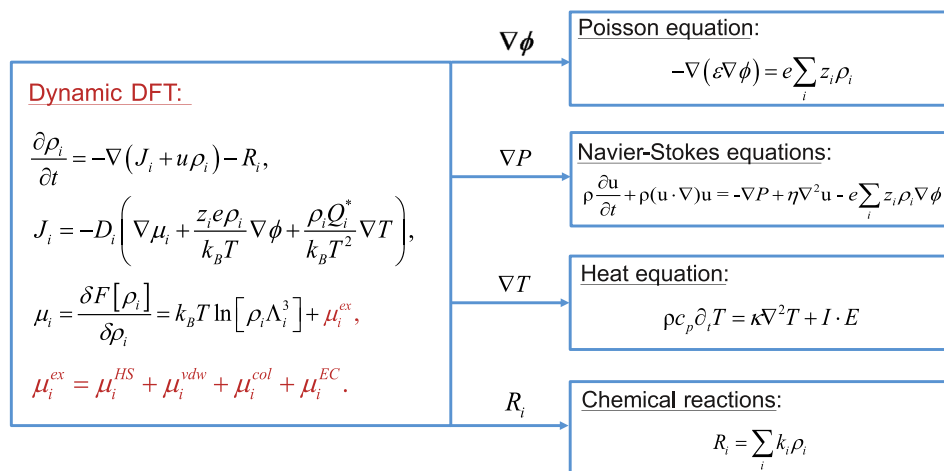
Fig. 13. Dynamic DFT theory for the nonequilibrium thermodynamics of electrolytes in porous electrodes.

through the comparison between kinetic and thermodynamic viewpoints [129]. Different from irreversible Joule heating which occurs everywhere in the electrolyte when charging, the reversible heating is originated from entropy change which is located in the EDL region near the electrode surface [130]. Reversely, Janssen had studied the response of electrical potential when a temperature quench was imposed in one electrode surface of a model electrolytic cell by solving the same coupled differential equations (Fig. 12b, **bottom**) [127]. The research demonstrated that for electrolytes with unequal ionic diffusivities, the relaxation of the thermo-voltage happens via a two-step process: a fast relaxation on the Debye timescale, followed by a slower diffusive relaxation, in agreement with experimental data of Bonetti et al. [131] When considering a reaction coupled system, e.g. electrochemical reduction of CO_2, the BV equations can be used to model the surface electrode reaction [124]:

$$i = i_0 \left[\exp\left(\frac{\alpha_a n F \eta}{RT} \right) - \exp\left(-\frac{\alpha_c n F \eta}{RT} \right) \right] \tag{26}$$

Where i_0 is the exchange current density, α_a and α_c are the dimensionless anodic and cathodic charge transfer coefficients, respectively; n is the number of electrons involved in the electrode reaction, F is the Faraday constant, and R is the gas constant. Based on the PNP-BV equations, the electric field, ionic concentration and current density near the tip of an electrode can be computed to describe the influence of the tip radius on the electrocatalytic CO_2 reduction (Fig. 12c, **top**) [93]. For the electrochemical system, a detailed understanding of transport in mesostructured electrodes is crucial for the design of porous electrodes. Suter and Haussener [132] constructed a 3D mass transport model utilizing the accurate electrode geometry to calculate local concentration distributions of solution species by considering the buffer reactions in the electrolyte and modeling local catalytic surface reaction rates based on BV correlations (Fig. 12c, **bottom**).

3.5. Perspective of DDFT

Despite the low computational cost and wide application compared with MD simulation, the PNP equations is based on the dilute solution theory that assumes point species, which is limited by the breaking of steric limit of ion concentration close to the charged surface at high applied voltages relative to the thermal voltage [133,134]. DDFT is a comprehensive method, which is equal to the Nernst−Planck (NP) equations when ignoring excess chemical potential. Free energy F can be divided into ideal free energy F^{id} and excess free energy F^{ex}. And Excess chemical potential (μ^{ex}), which is obtained from the partial derivation of F, can be divided into hard sphere contribution (μ^{HS}), van der Waals attraction (μ^{vdw}), Coulomb force (μ^{col}) and classical correlation term (μ^{EC}). DDFT can be coupled with several other partial differential equations including Poisson equation, NS equation, heat equation and BV equation, to study some interesting phenomena for porous electrode, which will be discussed in this section based on recent woks (as shown in Fig. 13).

3.5.1. Charging dynamics of porous electrodes ($\nabla \phi$)

As discussed above, the simulation of charging dynamics in EDLC with nanometer pores, which have been implemented in different methods ranging from MFT to MD simulations, still remains some difficulties. One of the main challenges is to combine the complex structures of porous electrodes [135]. It should also be noted that there are multiple distinct timescales that may be involved in charging dynamics [136,137]. Time scales in the sub-nanosecond region primarily reflect the diffusion of molecules; the millisecond regime can be understood in terms of an RC constant of the system [138]; and the timescale of seconds or longer are usually unexpected for processes in a liquid.

DDFT is an effective method to describe ionic steric effects and electrostatic correlations which are ignored in the PNP equation. Jiang et al. [139] studied the electrokinetic phenomena of ionic liquid EDL charging in slit-pores with the
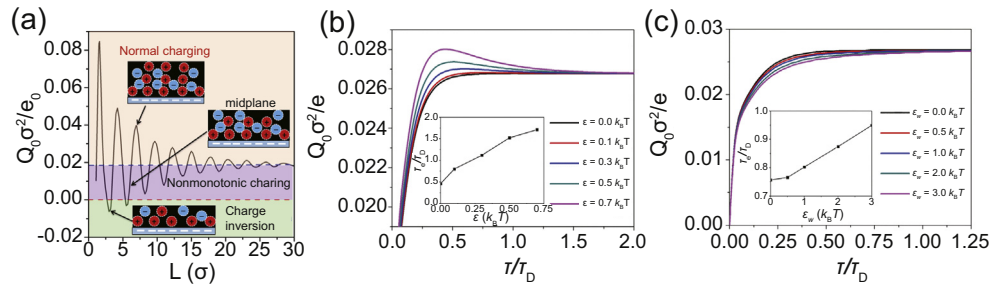
Fig. 14. **(a)** Dependence of surface charge density on the cell width obtained from CDFT. Reprinted with permission from Ref. [139]. Copyright (2014) American Physical Society. Time-dependent surface charge density under different strengths of **(b)** ion−ion dispersion forces and **(c)** wall-ion dispersion energy. (Inset) The equilibrium relaxation time as a function of dispersion energy. Reprinted with permission from Ref. [140]. Copyright (2016) AIP Publishing.
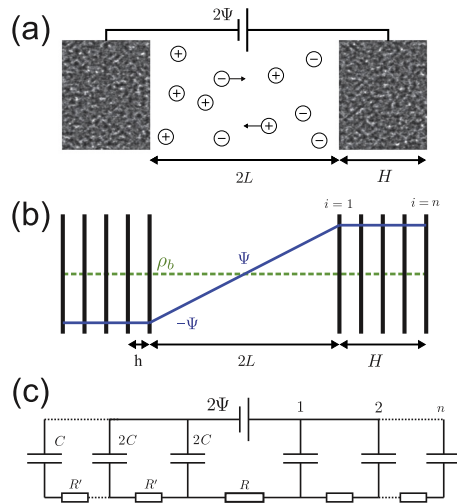

Numerical calculation:

$$\partial_x^2 \phi(x,t) = -\kappa^2 \left[\frac{\rho_+(x,t) - \rho_-(x,t)}{2\rho_b} \right];$$

$$\partial_t \rho_\pm(x,t) = -\partial_x j_\pm(x,t);$$
$$j_\pm(x,t) = -D\left[\partial_x \rho_\pm(x,t) \pm \rho_\pm(x,t)\partial_x \phi(x,t)\right].$$

Equivalent circuit model:

$$\begin{pmatrix} \Delta\dot{\Psi}_1(t) \\ \Delta\dot{\Psi}_2(t) \\ \Delta\dot{\Psi}_3(t) \\ \vdots \\ \Delta\dot{\Psi}_n(t) \end{pmatrix} = \frac{\Psi}{RC}\begin{pmatrix} 1 \\ 0 \\ \vdots \\ \vdots \\ 0 \end{pmatrix} - \frac{1}{2R'C}\begin{pmatrix} 1+\frac{H}{L(n-1)} & -1 & & & \\ -1 & 2 & -1 & & \\ & -1 & \ddots & \ddots & \\ & & \ddots & \ddots & -1 \\ & & & -1 & 2 & -1 \\ & & & & -2 & 2 \end{pmatrix}\begin{pmatrix} \Delta\Psi_1(t) \\ \Delta\Psi_2(t) \\ \Delta\Psi_3(t) \\ \vdots \\ \Delta\Psi_n(t) \end{pmatrix}$$

Both analytical and numerical methods gives:

$$\frac{\tau_n}{\tau_{RC}} = \left[2 + 0.75\frac{H}{L}\right]n - 1 - 0.91\frac{H}{L}.$$

Fig. 15. **(a)** Sketch of a supercapacitor with two porous electrodes. **(b)** Schematic representation of the stack-electrode model, in which both anode and cathode contain *n* planar electrodes with the intervals of *h*. **(c)** Equivalent circuit model for the stack-electrode model. Reprinted with permission from Ref. [141]. Copyright (2020) American Physical Society.

pore size varying from sub-nanometer to several nanometers (Fig. 14a). They showed three types of charging behavior, that is, normal charging, non-monotonic charging, and charge inversion, depending on the cell width and voltage. A later work by Lian et al. [140] extent the DDFT used in Ref. [139] By taking into account the dispersion forces, which is important for the bulk properties of RTILs. Due to the ion−ion dispersion, surface charge was shown to be a non-monotonic function of time (Fig. 14b). However, the electrode-ion dispersion interactions have no influence on the monotonic evolution of surface charge density as predicted by conventional PNP equation (Fig. 14c). Meanwhile, the duration of charging process was increased by both ion−ion and electrode-ion dispersion interactions.

Supercapacitors are electric energy storage devices containing a fluid with mobile ions that fill the nanometer-wide pores of porous electrodes. When the supercapacitor is charged, these mobile ions move towards and away from the electrode surface depending on the sign of their charge. The timescale with which these reconfigurations take place critically determines the power that the supercapacitor can later deliver. However, a wide gap still lies between experimentally measured and theoretically predicted timescales. To bridge this gap, Lian et al. [141] propose a simple electrode model (Fig. 15) that reproduces some of the salient features of supercapacitor charging while still being computationally accessible. Equivalent circuit model can describe the charging behavior of the stack-electrode model at low applied voltages. However, when the model was imposed with high potentials, charging dynamics slow down and evolve on two relaxation time scales: a generalized RC time and a diffusion time, which is similar with the experimental time scales of porous electrodes qualitatively. The stack-electrode model provides an effective approach to understand the charging dynamics of porous electrodes.

3.5.2. Electroosmotic flow in electrodes ($\Delta\phi$)

Electroosmotic flow in individual nanochannels, as the representative electrokinetic phenomenon, has been widely studied using different methods. However, due to the pore size distribution and pore connectivity of porous materials, the results for individual nanochannels is difficult to describe the ion transport in the porous structure. Lian et al. [142] used a multiscale approach to study ion transport in nanoporous materials, in which EDL structure was described by the classical DFT, fluid flow was calculated by the NS equation, and the gap between individual nanopores and porous network was
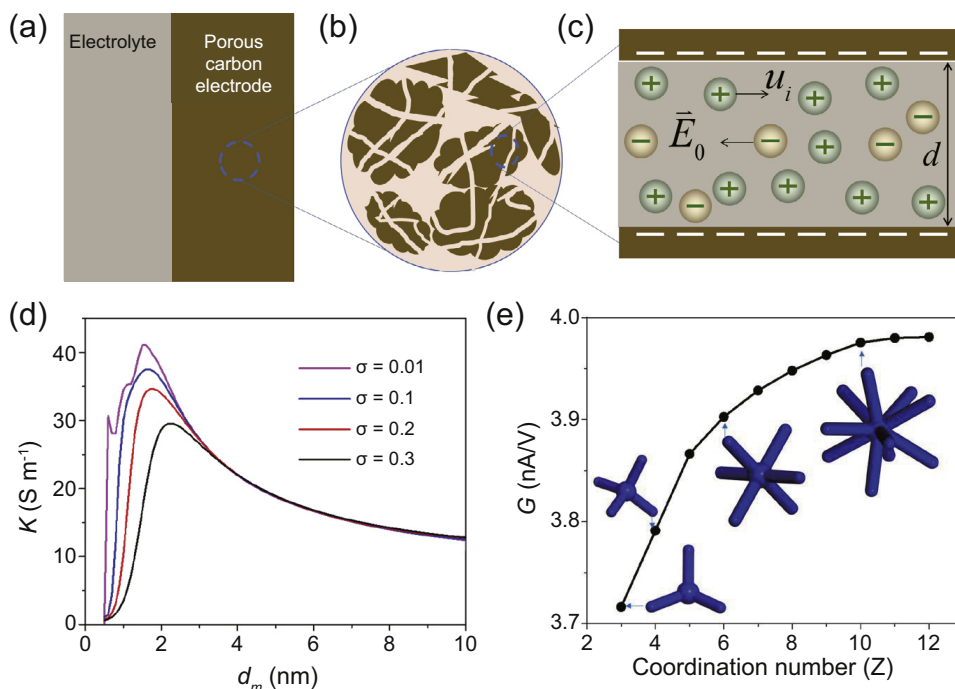
Fig. 16. **(a)** The interface between porous electrode material and electrolyte. **(b)** Schematic representation of microscopic structure for the porous material immersed in an electrolyte solution. **(c)** Schematic of ion transport through a negatively charged nanochannel of width d when an electric field was imposed. **(d)** The conductivity (K) of the electrolyte in porous electrodes as a function of average pore size with different pore size distributions σ. **(e)** The conductance (G) of the electrolyte in porous electrodes for different pore connectivity. Reprinted with permission from Ref. [142]. Copyright (2019) American Chemical Society.

bridged using the effective medium approximation (Fig. 16). The result demonstrated that pore size distribution had large influence on the ion conductivity in nanoporous materials when the average pore size is comparable to the EDL thickness. Based on the effective medium approximation method, the results from DFT calculation, MD simulation and continuum methods can be utilized to explore the ion transport in porous materials.
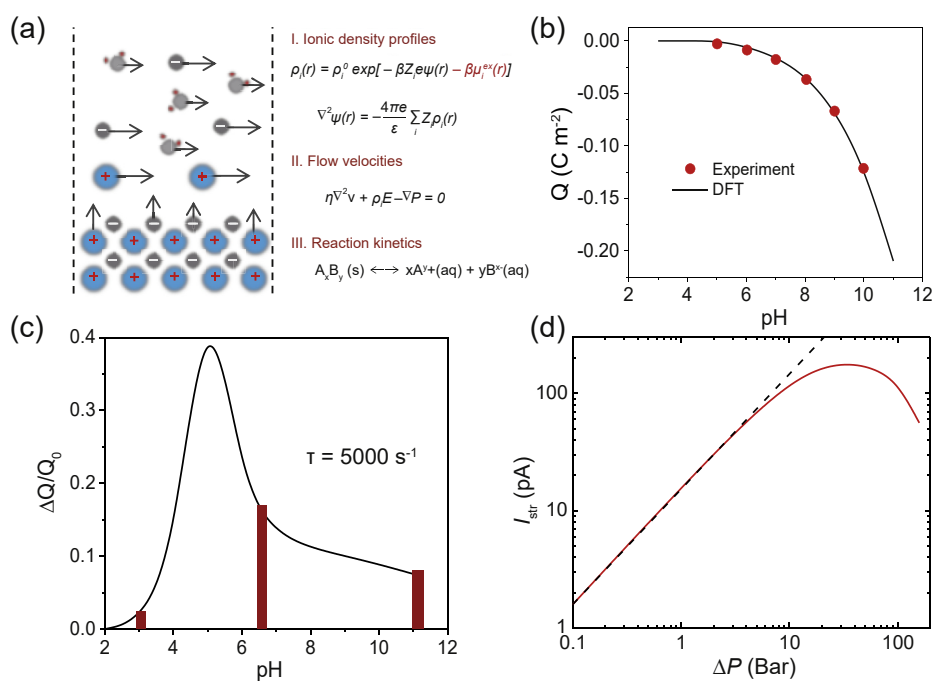

Fig. 17. **(a)** Model for the flow effect on the surface reactions. **(b)** Dependence of surface charge density Q on the pH without flow for SiO_2 substrate. **(c)** Change of surface charge density under the effect of flow with different pH. **(d)** Streaming current as a function of the pressure drop with pH = 6.5. Reprinted with permission from Ref. [143]. Copyright (2019) Royal Society of Chemistry.

3.5.3. Flow effects on the surface reaction ∇P

As discussed in section of experimental observation, fluid flow near a surface has a large influence on structure of surface water molecules and charges, but remain poorly understood from a molecular perspective. Lian et al. [143] studied the interaction between fluid flow and surface chemistry using a combined approach based on the CDFT method, NS equation, and reaction kinetics (Fig. 17a). The simulation result agrees well with experimental surface charge densities (Fig. 17b). The rate of surface reactions can be affected dramatically by the fluid flow near the surface, changing the structure of surface charges and water molecules (Fig. 17c), and thus leading to a nonlinear streaming current (Fig. 17d).

4. Conclusion and perspective

Energy storage and conversion devices such as lithium-ion batteries, fuel cells and supercapacitors are required as power battery systems with high power density, high energy density, high stability and high safety. However, the multi-phase transport and interfacial reaction processes of gases, liquids, ions, and electrons are high-nonlinearly coupled in hierarchical porous electrode materials, which make it difficult to investigate intrinsic rules quantitatively and establish general theories to guide the preparation of electrolyte and electrode materials.

This paper has reviewed the theoretical research methods and progress in studying the electrolyte structures in porous electrode or on the electrolyte–electrode interface for the electrochemical system, including classical density functional theory (CDFT), molecular simulation (MD), Grand Canonical Monte Carlo (GCMC), mean-field theory (MFT) and machine learning (ML), which greatly improves our understanding of the electrochemical behavior of electrolytes which can't be captured by experimental approaches.

Advanced in situ/operando experimental approaches are significant to investigate the complex transport and reaction processes in EDLC, pseudocapacitors, batteries. Despite the aforementioned impressive progress, the nonequilibrium ion transport in electrodes are still needed to develop for the novel energy storage devices with wide operational voltages and sufficient energy density while enhancing high power density and long cycle life, especially for large-scale energy-storage applications. The nanoscale nonequilibrium phenomena and nonequilibrium thermodynamics are totally different to that in the bulk, which are difficult to observe from experiments directly. Molecular theory and simulations have advantages on studying ionic transport and charging dynamics.

We summarize some perspectives and opportunities for future theoretical research methods for studying the nonequilibrium phenomena and nonequilibrium thermodynamics of electrolytes in porous electrodes.

(1) Considering the coupling effect of these irreversible processes mentioned above, the Onsager's reciprocal relation and linear response of traditional linear non-equilibrium

theory are introduced and developed. Onsager response matrix can be solved analytically to obtain the non-diagonal terms which describe the interactions between any two thermodynamic forces. As we know, it is not easy mathematically to obtain the analytical solutions of Onsager matrix. Even the analytical expressions are obtained, it only gives simple physical pictures which could facilitate our simple understanding of different processes and their relations.

(2) MD simulation is a good and common way to understand the nonequilibrium phenomena in porous material. The Onsager response matrix could be also solved by MD simulations. However, MD simulations are time-consuming and only applied for nanoscale system, more advanced MD simulation techniques should be developed for multiscale simulations.

(3) Besides, based on the Multiphysics coupling continuous method, different partial differential equations for describing corresponding transport processes are solved using finite element method to explore the dynamics of electrolytes in porous electrodes. However, the molecular-scale phenomena are not taken into account. More molecular details like more realistic molecular interactions should be considered.

(4) As an alternative to molecular dynamic (MD) or continuous methods, dynamic density functional theory (DDFT) is an efficient approach to describe the equilibrium and dynamic properties of many-body systems in terms of the one-body density profiles. The system parameters can be precisely tuned, and we can focus on the most important physical problems, using a computationally efficient coarse-grained approach to model real fluids. Further development of DDFT framework coupled with other thermodynamic forces would allow us to directly study the multi-physical processes of electrodes.

We hope that the methods mentioned above especially DDFT could provide mesoscale understanding of nonequilibrium phenomena in porous electrodes and guides the design and synthesis of electrode materials for high-performance lithium-ion batteries, fuel cell, supercapacitors, and pseudocapacitors.

Conflict of interest

The authors declare that they have no known competing financial interests or personal relationships that could have appeared to influence the work reported in this paper.

Acknowledgments

References

[1] Y. Li, Z.Y. Fu, B.L. Su, Adv. Funct. Mater. 22 (2012) 4634−4667.
[2] K. Jayaramulu, D.P. Dubal, B. Nagar, V. Ranc, O. Tomanec, M. Petr, K.K.R. Datta, R. Zboril, P. Gomez-Romero, R.A. Fischer, Adv. Mater. 30 (2018) e1705789.
[3] Y. Zhai, Y. Dou, D. Zhao, P.F. Fulvio, R.T. Mayes, S. Dai, Adv. Mater. 23 (2011) 4828−4850.
[4] M. Zhi, C. Xiang, J. Li, M. Li, N. Wu, Nanoscale 5 (2013) 72−88.
[5] E. Pomerantseva, F. Bonaccorso, X. Feng, Y. Cui, Y. Gogotsi, Science 366 (2019) eaan8285.
[6] Q. Wang, J. Yan, Z. Fan, Energy Environ. Sci. 9 (2016) 729−762.
[7] A. Burke, Electrochim. Acta 53 (2007) 1083−1091.
[8] X. Yang, C. Cheng, Y. Wang, L. Qiu, D. Li, Science 341 (2013) 534−537.
[9] Y. Xu, Z. Lin, X. Zhong, X. Huang, N.O. Weiss, Y. Huang, X. Duan, Nat. Commun. 5 (2014) 4554.
[10] S. Bose, T. Kuila, A.K. Mishra, R. Rajasekar, N.H. Kim, J.H. Lee, J. Mater. Chem. 22 (2012) 767−784.
[11] L.L. Zhang, X.S. Zhao, Chem. Soc. Rev. 38 (2009) 2520−2531.
[12] E. Frackowiak, F. Beguin, Carbon 39 (2001) 937−950.
[13] H. Jiang, J. Ma, C. Li, Adv. Mater. 24 (2012) 4197−4202.
[14] A. Balducci, R. Dugas, P.L. Taberna, P. Simon, D. Plee, M. Mastragostino, S. Passerini, J. Power Sources 165 (2007) 922−927.
[15] H.V. Helmholtz, Ann. Phys. 165 (1853) 353−377.
[16] Y. Wang, Y. Song, Y. Xia, Chem. Soc. Rev. 45 (2016) 5925−5950.
[17] F. Béguin, V. Presser, A. Balducci, E. Frackowiak, Adv. Mater. 26 (2014) 2219−2251.
[18] J. Wang, S. Kaskel, J. Mater. Chem. 22 (2012) 23710−23725.
[19] A. Vu, Y. Qian, A. Stein, Adv. Energy Mater. 2 (2012) 1056−1085.
[20] Z.S. Wu, W. Ren, L. Wen, L. Gao, J. Zhao, Z. Chen, G. Zhou, F. Li, H.M. Cheng, ACS Nano 4 (2010) 3187−3194.
[21] H.J. Song, D.S. Kim, J.C. Kim, S.H. Hong, D.W. Kim, J. Mater. Chem. 5 (2017) 5502−5510.
[22] L.E. Shea-Rohwer, J.E. Martin, X. Cai, D.F. Kelley, ECS J. Solid State Sci. Technol. 2 (2013) R3112−R3118.
[23] D. Lei, J. Benson, A. Magasinski, G. Berdichevsky, G. Yushin, Science 355 (2017) 267−271.
[24] F. Xu, L. Wu, Q. Meng, M. Kaltak, J. Huang, J.L. Durham, M. Fernandezserra, L. Sun, A.C. Marschilok, E.S. Takeuchi, Nat. Commun. 8 (2017) 15400.
[25] S.L. Candelaria, Y.Y. Shao, W. Zhou, X.L. Li, J. Xiao, J.G. Zhang, Y. Wang, J. Liu, J.H. Li, G.Z. Cao, Nanomater. Energy 1 (2012) 195−220.
[26] O.C. Compton, S.T. Nguyen, Small 6 (2010) 711−723.
[27] F. Li, X. Jiang, J. Zhao, S. Zhang, Nanomater. Energy 16 (2015) 488−515.
[28] B. Anasori, M.R. Lukatskaya, Y. Gogotsi, Nat. Rev. Mater. 2 (2017) 16098.
[29] J. Tang, R.R. Salunkhe, J. Liu, N.L. Torad, M. Imura, S. Furukawa, Y. Yamauchi, J. Am. Chem. Soc. 137 (2015) 1572−1580.
[30] W. Xia, A. Mahmood, R. Zou, Q. Xu, Energy Environ. Sci. 8 (2015) 1837−1866.
[31] J.K. Sun, Q. Xu, Energy Environ. Sci. 7 (2014) 2071−2100.
[32] P. Pachfule, D. Shinde, M. Majumder, Q. Xu, Nat. Chem. 8 (2016) 718.
[33] D. Sheberla, J.C. Bachman, J.S. Elias, C.J. Sun, Y. Shao-Horn, M. Dincă, Nat. Mater. 16 (2017) 220−224.
[34] Y. Mao, G. Li, Y. Guo, Z. Li, C. Liang, X. Peng, Z. Lin, Nat. Commun. 8 (2017) 14628.
[35] H. Hu, Z. Zhao, Y. Gogotsi, J. Qiu, Environ. Sci. Technol. Lett. 1 (2014) 214−220.
[36] A.D. Aikens, J. Chem. Educ. 60 (1983) A25.
[37] J.Z. Wu, Z.D. Li, Annu. Rev. Phys. Chem. 58 (2007) 85−112.
[38] D.E. Jiang, Z. Jin, D. Henderson, J. Wu, J. Phys. Chem. Lett. 3 (2012) 1727−1731.
[39] D.E. Jiang, J. Wu, Nanoscale 6 (2014) 5545−5550.
[40] R. Evans, Adv. Phys. 28 (1979) 143−200.
[41] R. Evans, M. Oettel, R. Roth, G. Kahl, J. Phys. Condens. Matter 28 (2016) 240401.
[42] A. Haghmoradi, L. Wang, W.G. Chapman, J. Phys. Condens. Matter 28 (2016) 244009.
[43] C. Lian, X. Chen, S. Zhao, W. Lv, X. Han, H. Wang, H. Liu, Macromol. Theory Simul. 23 (2014) 575−582.
[44] D.E. Jiang, J. Wu, J. Phys. Chem. Lett. 4 (2013) 1260−1267.
[45] C. Lian, D.E. Jiang, H. Liu, J. Wu, J. Phys. Chem. C 120 (2016) 8704−8710.
[46] D.E. Jiang, M. Dong, J. Wu, Chem. Phys. Lett. 504 (2011) 153−158.
[47] D.E. Jiang, Z. Jin, J. Wu, Nano Lett. 11 (2011) 5373−5377.
[48] K. Ma, C. Lian, C.E. Woodward, B. Qin, Chem. Phys. Lett. 739 (2020) 137001.
[49] C. Lian, X. Kong, H. Liu, J. Wu, J. Phys. Condens. Matter 28 (2016) 464008.
[50] C. Lian, H. Liu, D. Henderson, J. Wu, J. Phys. Condens. Matter 28 (2016) 414005.
[51] C. Lian, C. Zhan, D.E. Jiang, H. Liu, J. Wu, J. Phys. Chem. C 121 (2017) 14010−14018.
[52] H. Su, C. Lian, A. Gallegos, S. Deng, Y. Shang, H. Liu, J. Wu, Chem. Eng. Sci. 215 (2020) 115452.
[53] C. Lian, H. Liu, C. Li, J. Wu, AIChE J. 65 (2019) 804−810.
[54] C. Lian, H. Liu, J. Wu, J. Phys. Chem. C 122 (2018) 18304−18310.
[55] C. Lian, K. Liu, K.L. van Aken, Y. Gogotsi, D.J. Wesolowski, H. Liu, D. Jiang, J. Wu, ACS Energy Lett. 1 (2016) 21−26.
[56] C. Lian, H. Su, H. Liu, J. Wu, J. Phys. Chem. C 122 (2018) 14402−14407.
[57] Y. Qiu, Y. Chen, J. Phys. Chem. C 119 (2015) 23813−23819.
[58] G. Feng, R. Qiao, J. Huang, B.G. Sumpter, V. Meunier, ACS Nano 4 (2010) 2382−2390.
[59] G. Feng, S. Li, W. Zhao, P.T. Cummings, AIChE J. 61 (2015) 3022−3028.
[60] J.L. BanUelos, G. Feng, P.F. Fulvio, S. Li, G. Rother, S. Dai, P.T. Cummings, D.J. Wesolowski, Chem. Mater. 26 (2014) 1144−1153.
[61] J.I. Siepmann, M. Sprik, J. Chem. Phys. 102 (1995) 511−524.
[62] L. Pastewka, T.T. Järvi, L. Mayrhofer, M. Moseler, Phys. Rev. B 83 (2011) 165418.
[63] C. Merlet, C. Péan, B. Rotenberg, P.A. Madden, P. Simon, M. Salanne, J. Phys. Chem. Lett. 4 (2013) 264−268.
[64] J.B. Haskins, J.W. Lawson, J. Chem. Phys. 144 (2016) 184707.
[65] B.L. Bhargava, S. Balasubramanian, M.L. Klein, Chem. Commun. (2008) 3339−3351.
[66] C. Merlet, M. Salanne, B. Rotenberg, P.A. Madden, J. Phys. Chem. C 115 (2011) 16613−16618.
[67] Z. Liu, X. Wu, W. Wang, Phys. Chem. Chem. Phys. 8 (2006) 1096−1104.
[68] N.M. Micaelo, A.M. Baptista, C.M. Soares, J. Phys. Chem. B 110 (2006) 14444−14451.
[69] J. Vatamanu, O. Borodin, G.D. Smith, J. Am. Chem. Soc. 132 (2010) 14825−14833.
[70] J.N.C. Lopes, A.A.H. Pádua, Theor. Chem. ACC. 131 (2012) 1129.
[71] K. Kiyohara, K. Asaka, J. Chem. Phys. 126 (2007) 214704.
[72] K. Kiyohara, K. Asaka, J. Phys. Chem. C 111 (2007) 15903−15909.
[73] S.R. Varanasi, S.K. Bhatia, J. Phys. Chem. C 119 (2015) 17573−17584.
[74] S.R. Varanasi, A.H. Farmahini, S.K. Bhatia, J. Phys. Chem. C 119 (2015) 28809−28818.
[75] M. Jitvisate, J.R.T. Seddon, J. Phys. Chem. Lett. 9 (2018) 126−131.
[76] M.V. Fedorov, A.A. Kornyshev, Chem. Rev. 114 (2014) 2978−3036.
[77] M.Z. Bazant, B.D. Storey, A.A. Kornyshev, Phys. Rev. Lett. 106 (2011) 046102.
[78] A.A. Kornyshev, J. Phys. Chem. B 20 (2007) 5545−5557.
[79] M. Zhou, A. Gallegos, K. Liu, S. Dai, J. Wu, Carbon 157 (2020) 147−152.
[80] J. Wang, X. Zhang, Z. Li, Y. Ma, L. Ma, J. Power Sources 451 (2020) 227794.
[81] H. Sui, L. Li, X. Zhu, D. Chen, G. Wu, Chemosphere 144 (2016) 1950−1959.
[82] P. Mccullagh, J.A. Nelder, in: Monographs on Statistics & Applied Probability, second ed., Chapman and Hall/CRC, UK, 1989.

[83] A.J. Smola, B. Scholkopf, Stat. Comput. 14 (2004) 199−222.
[84] S. Zhu, J. Li, L. Ma, C. He, E. Liu, F. He, C. Shi, N. Zhao, Mater. Lett. 233 (2018) 294−297.
[85] J.H. Lee, J. Shin, M.J. Realff, Comput. Chem. Eng. 114 (2017) 111−121.
[86] M. Popescu, V.E. Balas, L. Perescupopescu, N.E. Mastorakis, WSEAS Transact. Circuits Syst. 8 (2009) 579−588.
[87] H. Su, S. Lin, S. Deng, C. Lian, Y. Shang, H. Liu, Nanoscale Adv. 1 (2019) 2162−2166.
[88] H. Su, C. Lian, J. Liu, H. Liu, Chem. Eng. Sci. 202 (2019) 186−193.
[89] A.A. Franco, A. Rucci, D. Brandell, C. Frayret, M. Gaberscek, P. Jankowski, P. Johansson, Chem. Rev. 119 (2019) 4569−4627.
[90] S. Pannala, J.A. Turner, S. Allu, W.R. Elwasif, S. Kalnaus, S. Simunovic, A. Kumar, J.J. Billings, H. Wang, J. Nanda, J. Appl. Phys. 118 (2015) 072017.
[91] Y. Demirel, V. Gerbaud, in: Y. Demirel, V. Gerbaud (Eds.), Nonequilibrium Thermodynamics, fourth ed., Elsevier, United States, 2019, pp. 135−186.
[92] P.B. Peters, R. Van Roij, M.Z. Bazant, P.M. Biesheuvel, Phys. Rev. 93 (2016) 053108.
[93] M. Liu, Y. Pang, B. Zhang, P.D. Luna, O. Voznyy, J. Xu, X. Zheng, C.T. Dinh, F. Fan, C. Cao, F.P.G. de Arquer, T.S. Safaei, A. Mepham, A. Klinkova, E. Kumacheva, T. Filleter, D. Sinton, S.O. Kelley, E.H. Sargent, Nature 537 (2016) 382−386.
[94] S.M. Chathoth, E. Mamontov, A.I. Kolesnikov, Y. Gogotsi, D.J. Wesolowski, Europhys. Lett. 95 (2011) 56001.
[95] N.C. Osti, A. Cote, E. Mamontov, A.J. Ramirezcuesta, D.J. Wesolowski, S. Diallo, Chem. Phys. 465−466 (2016) 1−8.
[96] D. Chung, N. Balke, S.V. Kalinin, R.E. Garcia, J. Electrochem. Soc. 158 (2011) A1083−A1089.
[97] A.N. Morozovska, E.A. Eliseev, N. Balke, S.V. Kalinin, J. Appl. Phys. 108 (2010) 053712.
[98] S. Jesse, N. Balke, E.A. Eliseev, A. Tselev, N.J. Dudney, A.N. Morozovska, S.V. Kalinin, ACS Nano 5 (2011) 9682−9695.
[99] T.M. Fears, M. Doucet, J.F. Browning, J.K. Baldwin, J.G. Winiarz, H. Kaiser, H. Taub, R.L. Sacci, G.M. Veith, Phys. Chem. Chem. Phys. 18 (2016) 13927−13940.
[100] S. Li, J.L. Banuelos, J. Guo, L.M. Anovitz, G. Rother, R.W. Shaw, P.C. Hillesheim, S. Dai, G.A. Baker, P.T. Cummings, J. Phys. Chem. Lett. 3 (2012) 125−130.
[101] Z. Lin, P. Rozier, B. Duployer, P. Taberna, B. Anasori, Y. Gogotsi, P. Simon, Electrochem. Commun. 72 (2016) 50−53.
[102] J.M. Black, G. Feng, P.F. Fulvio, P.C. Hillesheim, S. Dai, Y. Gogotsi, P.T. Cummings, S.V. Kalinin, N. Balke, Adv. Energy Mater. 4 (2014) 1−8.
[103] J.M. Black, M.B. Okatan, G. Feng, P.T. Cummings, N. Balke, Nanomater. Energy 15 (2015) 737−745.
[104] J. Black, G. Feng, P.F. Fulvio, P.C. Hillesheim, S. Dai, Y. Gogotsi, P.T. Cummings, S.V. Kalinin, N. Balke, Adv. Energy Mater. 4 (2014) 1300683.
[105] J.L. Achtyl, I. Vlassiouk, S. Dai, F.M. Geiger, J. Phys. Chem. C 118 (2014) 17745−17755.
[106] J.L. Achtyl, I. Vlassiouk, S.P. Surwade, P.F. Fulvio, S. Dai, F.M. Geiger, J. Phys. Chem. B 118 (2014) 7739−7749.
[107] M. Deschamps, E. Gilbert, P. Azais, E. Raymundopinero, M.R. Ammar, P. Simon, D. Massiot, F. Beguin, Nat. Mater. 12 (2013) 351−358.
[108] F. Blanc, M. Leskes, C.P. Grey, Acc. Chem. Res. 46 (2013) 1952−1963.

[109] D. Lis, E.H.G. Backus, J. Hunger, S.H. Parekh, M. Bonn, Science 344 (2014) 1138−1142.
[110] M. Janssen, E. Griffioen, P.M. Biesheuvel, R. van Roij, B. Erné, Phys. Rev. Lett. 119 (2017) 166002.
[111] B.L. Werkhoven, R. van Roij, Soft Matter 16 (2020) 1527−1537.
[112] R. Qiao, N.R. Aluru, Phys. Rev. Lett. 92 (2004) 198301.
[113] O.N. Kalugin, V.V. Chaban, V.V. Loskutov, O.V. Prezhdo, Nano Lett. 8 (2008) 2126−2130.
[114] J. Su, D. Huang, J. Phys. Chem. C 120 (2016) 11245−11252.
[115] S. Delmerico, J.G. Mcdaniel, Carbon 161 (2020) 550−561.
[116] S. Kondrat, P. Wu, R. Qiao, A.A. Kornyshev, Nat. Mater. 13 (2014) 387−393.
[117] K. Breitsprecher, C. Holm, S. Kondrat, ACS Nano 12 (2018) 9733−9741.
[118] T. Mo, S. Bi, Y. Zhang, V. Presser, X. Wang, Y. Gogotsi, G. Feng, ACS Nano 14 (2020) 2395−2403.
[119] L. Fu, L. Joly, S. Merabia, Phys. Rev. Lett. 123 (2019) 138001.
[120] H. Yoshida, S. Marbach, L. Bocquet, J. Chem. Phys. 146 (2017) 194702.
[121] M.Z. Bazant, Acc. Chem. Res. 46 (2013) 1144−1160.
[122] E. Karimi-Sibaki, A. Kharicha, M. Wu, A. Ludwig, J. Bohacek, Ionics 24 (2018) 2157−2165.
[123] I. Sprague, P. Dutta, Electrochim. Acta 56 (2011) 4518−4525.
[124] A.J. Bard, L.R. Faulkner, in: Electrochemical Methods, Fundamentals & Applications, second ed., John Wiley & Sons, Inc., New York, 2001.
[125] H. Tao, S. Lin, C. Lian, C. Li, H. Liu, Chem. Eng. Sci. 212 (2020) 115354.
[126] M. Dietzel, S. Hardt, Phys. Rev. Lett. 116 (2016) 225901.
[127] M. Janssen, M. Bier, Phys. Rev. 99 (2019) 042136.
[128] R.F. Stout, A.S. Khair, Phys. Rev. 96 (2017) 022604.
[129] M. Janssen, R. van Roij, Phys. Rev. Lett. 118 (2017) 096001.
[130] J. Schiffer, D. Linzen, D.U. Sauer, J. Power Sources 160 (2006) 765−772.
[131] M. Bonetti, S. Nakamae, B.T. Huang, T.J. Salez, C. Wiertel-Gasquet, M. Roger, J. Chem. Phys. 142 (2015) 244708.
[132] S. Suter, S. Haussener, Energy Environ. Sci. 12 (2019) 1668−1678.
[133] M. Mirzadeh, F. Gibou, T.M. Squires, Phys. Rev. Lett. 113 (2014) 097701.
[134] J. Lyklema, in: Fundamentals of Interface and Colloid Science: Solid-liquid Interfaces, first ed., Academic Press, London, 1995.
[135] A.C. Forse, C. Merlet, J.M. Griffin, C.P. Grey, J. Am. Chem. Soc. 138 (2016) 5731−5744.
[136] A. Uysal, H. Zhou, G. Feng, S.S. Lee, S. Li, P.T. Cummings, P.F. Fulvio, S. Dai, J.K. Mcdonough, Y. Gogotsi, J. Phys. Condens. Matter 27 (2015) 032101.
[137] G. Wang, W. Brown, M. Kvetny, Curr. Opin. Electrochem. 13 (2019) 112−118.
[138] C. Pean, C. Merlet, B. Rotenberg, P.A. Madden, P.L. Taberna, B. Daffos, M. Salanne, P. Simon, ACS Nano 8 (2014) 1576−1583.
[139] J. Jiang, D. Cao, D. Jiang, J. Wu, J. Phys. Chem. Lett. 5 (2014) 2195−2200.
[140] C. Lian, S. Zhao, H. Liu, J. Wu, J. Chem. Phys. 145 (2016) 204707.
[141] C. Lian, M. Janssen, H. Liu, R. van Roij, Phys. Rev. Lett. 124 (2020) 076001.
[142] C. Lian, H. Su, C. Li, H. Liu, J. Wu, ACS Nano 13 (2019) 8185−8192.
[143] C. Lian, X. Kong, H. Liu, J. Wu, Phys. Chem. Chem. Phys. 21 (2019) 6970−6975.